GROWTH AND CHARACTERIZATION OF MAGNETIC MnSb NANOSTRUCTURES

ZHANG HONGLIANG

(B. Eng. Shandong University, China)

A THESIS SUBMITTED

FOR THE DEGREE OF MASTER OF SCIENCE

DEPARTMENT OF PHYSICS

NATIONAL UNIVERSITY OF SINGAPORE

2008

ACKNOWLEDGEMENT

Many people have contributed to the efforts that made it possible to complete this dissertation and due to limited space only I can mention few of them; here is my appreciation to all of them.

First and foremost, I would like to express my deep sense of gratitude and sincere to my supervisors, Professor Andrew Wee T. S. and Associate Professor Xue-Sen Wang, for their inspiration, guidance and encouragement throughout the course of my work. All their invaluable suggestion and friendly personality will be always kept in my memory. It has been a truly rewarding experience to have the opportunity to work under their guidance.

Thanks are due to Dr Chen Wei， Dr Xu Hai and Dr. Gao Xingyu for their invaluable suggestion and continuous encouragement for my research works, especially to Dr. Chen Wei for his encouragement, support and generosity in expertise, time and discussion.

I also thank all group members and my friends, Dr. S. S. Kushvaha, Dr. Chen Lan, Dr. Wang Li, Mr. Wong How Kwong, Mr. Ho Kok Wen, Mr. Chu Xinjun, Mr. Huang Han, Miss Huang Yuli, Mr. Yong Chaw Keong, Mr. Chen Shi, Mr. Qi Dongchen, Mr. Zheng Yi, Mr. Zhang Ce, Miss Poon Siew Wai, Miss Yong Zhihua and all other Surface Science Lab. members for the pleasant moments experienced during my study.

I am grateful to National University of Singapore (NUS) and Department of Physics for providing me the research scholarship and grants to conferences.

Last but not least, my deep appreciation to my wife, my parents and my sister for their endless love, unceasing encouragement and thoughtful consideration.

CONTENTS

Summary

In recent years, magnetic nanostructures (magnetic ultrathin layers, magnetic nanowires and magnetic nanoparticls etc.) have been bringing revolutionary changes in device applications, especially in high-density data storage and spintronic-based devices. Among various magnetic materials, manganese based compounds, such as maganese pnictides，chalcogenides and their alloys, have received considerable attention, due to their attractive magnetic and magneto-optical properties.

The overall objective of this thesis is to study the growth and physical properties, i.e. morphological, structural, chemical and magnetic properties of various MnSb nanostructures on different substrates such as HOPG, Si(111) and SiNx. We investigated the growth behavior and the surface morphologies of MnSb nanostructures on these substrates in ultrahigh vacuum conditions by using *in situ scanning tunneling microscopy*. In particular, MnSb nano-crystallites and thin films were obtained on HOPG substrate by controlling the growth conditions. The MnSb thin film surface exhibits 2×2 and ($2\sqrt{3}\times 2\sqrt{3}$)R30° reconstructions on the MnSb(0001) surface, and a 2×1 superstructure on MnSb($10\bar{1}1$). VSM measurement revealed that the MnSb film was ferromagnetic at room temperature with a high saturation magnetization.

We also investigated the properties of MnSb nanoparticles self-assembled on Si-based substrates. More specifically, when MnSb was grown on Si(111) substrate, an Mn silicide layer could be easily formed by interfacial reaction between Mn and Si , which degraded the functionalities of both the substrate and the magnetic overlayer. However, by pre-depositing a ultrathin SiNx layers, MnSb nanoparticles with diameters $\langle d \rangle$ from 5 to 30 nm could be self-assembled on SiNx/Si(111) with sharp interface. Magnetic measurements indicate that MnSb particles with $\langle d \rangle < 9$ nm were superparamagnetic, while those with $\langle d \rangle \geq 15$ nm exhibited ferromagnetism at room temperature. These magnetic nanoparticles may offer the potential of integrating novel magnetic or spintronic functions on the widely used Si-based circuits.

ABBREVIATIONS

1-D	One-dimensional
2-D	Two-dimensional
3-D	Three-dimensional
AES	Aüger electron spectroscopy
XPS	X-ray photoelectron spectroscopy
XAS	X-ray absorption spectroscopy
HOPG	Highly oriented pyrolytic graphite
LEED	Low electron energy diffraction
NPs	Nanoparticles
NWs	Nanowires
RT	Room temperature
STM	Scanning tunneling microscopy
TEM	Transmission electron microscopy
UHV	Ultra-high vacuum
VSM	Vibrating sample magnetometer
V-W	Volmer-Weber

List of Figures

List of Publications

1. Hongliang Zhang, Wei Chen, Han Huang, Lan Chen, Andrew Thye Shen Wee, *"Preferential trapping of C_{60} in nanomesh voids"* ***J. Am. Chem. Soc.*** 130, 2720 (2008).

2. Lan Chen, Wei Chen, Han Huang, Hongliang Zhang, Andrew Thye Shen Wee, "*Tunable C_{60} molecular arrays"* ***Adv. Mater.*** 20, 484 (2008).

3. Han Huang, Wei Chen, Lan Chen, Hongliang Zhang, Xue Sen Wang, Shining Bao, and Andrew T. S. Wee, "*"Zigzag" C_{60} chain arrays*" ***Appl. Phys. Lett***. 92, 023105 (2008)

4. Hongliang Zhang, Wei Chen, Lan Chen, Han Huang, Xue Sen Wang, Andrew Thye Shen Wee, "*C_{60} molecular wire arrays on 6T nanostripes"* ***Small*** 3, 2015 (2007).

5. Wei Chen, Shi Chen, Hongliang Zhang, Hai Xu, Dongchen Qi, Xingyu Gao, Kian Ping Loh and Andrew T. S. Wee, "*Probing the interaction at the C60–SiC nanomesh interface"* ***Surf. Sci.*** 601, 2994 (2007).

6. Hongliang Zhang, Sunil S. Kushvaha, Shi Chen, Xingyu Gao, Dongchen Qi, Andrew T. S. Wee, and Xue-sen Wang, *"Synthesize and characterization of MnSb nanoparticles on Si-based substrates"* ***Appl. Phys. Lett.*** 90, 202503 (2007).

7. Hongliang Zhang, Sunil S. Kushvaha, Andrew T. S. Wee, and Xue-sen Wang "*Morphology, surface structures and magnetic properties of MnSb thin films and nanocrystallites grown on graphite"* ***J. Appl. Phys.*** 102, 023906 (2007).

8. Wei Chen, Han Huang, Shi Chen, Lan Chen, Hong Liang Zhang, Xing Yu Gao, and Andrew T. S. Wee, "*Molecular Orientation of PTCDA Thin Films at Organic Heterojunction Interfaces*" ***Appl. Phys. Lett.*** 91, 114102 (2007).

9. S.S. Kushvaha, Hai Xu, Hongliang Zhang, Andrew T.S. Wee, and Xuesen Wang

Shape-controlled Growth of Indium and Aluminum Nanostructures on MoS_2(0001) ***Journal of Nanoscience and Nanotechnology*** (In press).

10. Wei Chen, Hongliang Zhang, Hai Xu, Eng Soon Tok, Loh Kian Ping and Andrew T. S. Wee, "*C60 on SiC Nanomesh"* ***J. Phys. Chem. B,*** **110,** 21873-21881 (2006).

11. Wei Chen, Chun Huang, Xingyu Gao, Li Wang, C G Zhen, Dongchen Qi, Shi Chen, Hongliang Zhang, K P Loh, Z Chen, Andrew T S Wee, "*Tuning Hole Injection Barrier at the Organic/Metal Interface with Self-Assembled Functionalized Aromatic Thiols"* ***J. Phys. Chem. B,*** 110, 26075 (2006).

Chapter 1

Introduction

1.1 Nanostructures

Nanostructure refers to material systems with at least one dimension falling into the nanometer scale (~1-100 nm). Such nanoscale structures have drawn steadily growing attention as a result of their extraordinary functional properties and potential applications for further device miniaturization [1-4]. Over the past decades, we have witnessed marvelous advances in our ability to synthesize nanostructures of all types, as well as the development of novel experimental methods that allow us to explore their physical properties [5-7].

Nanostructures usually possess unique properties as compared with both individual atoms/molecules and their bulk counterparts. This is so because either a large fraction of their atomic or molecular constituents reside in surface sites of low symmetry, or their physical size is so small that quantum confinement effect dominates. The physical and chemical states of the atoms or molecules in the surface sites can be quite different from those of interior atoms, which lead to the dramatic changes in the physical and chemical properties of the nanostructures. For example, in the case of cobalt cluster on Pt(111) [8], orbital moment and magnetic anisotropy energy increase remarkably as the cluster size decreases.

Furthermore, because of the large surface area, nanostructures usually possess a high surface energy and, thus, are thermodynamically unstable or metastable. To overcome the surface energy barrier is also one challenge in fabrication and processing of nanostructures. Due to the reduced dimensions, electrons in nanostructures are confined in the nanoscale dimensions but are free to move in other dimensions. The wave function of electrons is going to change when they are confined to dimensions comparable with their wavelength. The quantum confinement of electrons results in quantization of energy and momentum, which dramatically change the band structure of nanostructural materials. Figure 1.1 shows the density of states of the low-dimensional structures. The density of states of the nanostructures is dramatically changed due to the quantum confinement effect. It is believed that a variety of striking phenomena in nanostructures, such as size-dependent excitation or emission [9], Coulomb blockade [10], resonant tunneling effect, and metal-insulator transition [11], are associated with the confinement of electrons in nanostructures. Basically, nanostructures can be classified into three types based on the dimensions in which the electrons are confined:

1) Two-dimensional (2D) nanostructures or quantum wells: electrons are confined in one dimension, free in other two dimensions. The 2D nanostructures can be realized by sandwiching a thin layer (a few nanometers) of narrow bandgap

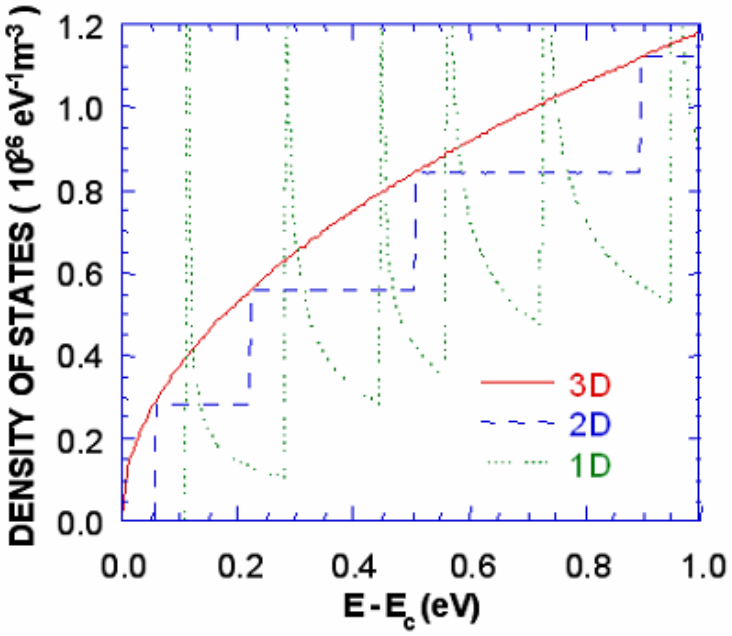

Figure 1.1 Density of states of nanostructures with different dimensions. Electrons confined to nanostructures give rise to low-dimensional quantum well states, which modify the density of states. States at the Fermi level trigger electronic phase transitions, such as magnetism and superconductivity.

semiconductor between that with a wider bandgap [12], such as a thin layer of GaAs sandwiched between two AlGaAs layers. Those architectures can be routinely prepared using conventional molecular beam epitaxy (MBE) technique. Because of the quantum confinement effect, the bandgap of the semiconductor (GaAs) is increased (blue-shift) by certain amount determined by the width of quantum wells. As a result the emission wavelength of the laser or light emitting

diode (LED) made of this kind of structure can be tuned by the width of the quantum well of GaAs.

2) One-dimensional (1D) nanostructures: electrons are confined in two dimensions, free in one dimension. Recently, 1D nanostructures such as nanowires, nanorods and nanotubes have been intensively investigated owing to their high potential in applications. For examples, carbon nanotubes (CNT) could be explored as building blocks to fabricate nanoelectronic devices (e.g., field effect transistors [13], p-n junctions [14]). Si and Ge [15,16], Goup III-V (GaN, GaAs and GaP *etc.*) [17, 18] and Group II-VI (ZnO, ZnSe and CdSe *etc.*) [19, 20] nanowires have been extensively studied for making electronic and optoelectronic devices.

3) Zero-dimensional (0D) nanostructures or quantum dots: electrons are confined in all three dimensions. 0D nanostructures include nanoparticles and clusters. The size, shape and orientation of nanoparticles or clusters are important to their thermal, electrical, chemical, optical and magnetic properties. With quantum dots as model system, scientists have learned a lot of interesting underlying science by studying the evolution of their properties with size. Typical 0D nanostructures studied include metallic nanoparticles (Au, Ag, Co, Cu, Fe, Pd, Pt, Rh *etc.*) [5, 21, 22], semiconductor quantum dots (Si, Ge, GaN, GaAs InAs, CdSe, ZnSe *etc.*) [23-31], and magnetic nanoparticles (Co, Ni, Fe, FePt, MnAs,

MnSb e*tc.*) [8, 31-38]. In Chapter 5, we will discuss the fabrication and magnetic properties of MnSb nanoparticles with controlled sizes.

1.2 Self-assembly of Nanostructures

As mentioned above, the properties of nanostructures depend sensitively on their size, shape and atomic arrangement. In order to explore novel physical properties and realize potential applications of nanostructures, the ability to fabricate nanostructures with controlled configuration is highly desirable. There are generally two approaches to fabricate nanostructures: "top-down" and "bottom-up" techniques [39-41], as shown in Figure 1.2 [41]. The "top-down" may rely on the traditional methods such as lithography, writing or stamping, capable of creating features down to the 100 nm range. The sophisticated tools allowing such precision are electron-beam writing and advanced lithographic techniques using extreme ultraviolet or soft X-ray radiation [42]. The limitations of "top-down" technique are its low resolution and damage to the materials. The "bottom-up" technique refers to the build-up of nanostructural architectures from bottom: atoms by atoms, molecules by molecules, or cluster-by-cluster [40, 43, 44]. For example, in crystal growth, growth species such as atoms, ions and molecules, after impinging onto the growth surface, assemble into crystal structure one after another (e.g., MBE growth of InAs nanodots on GaAs [45]).

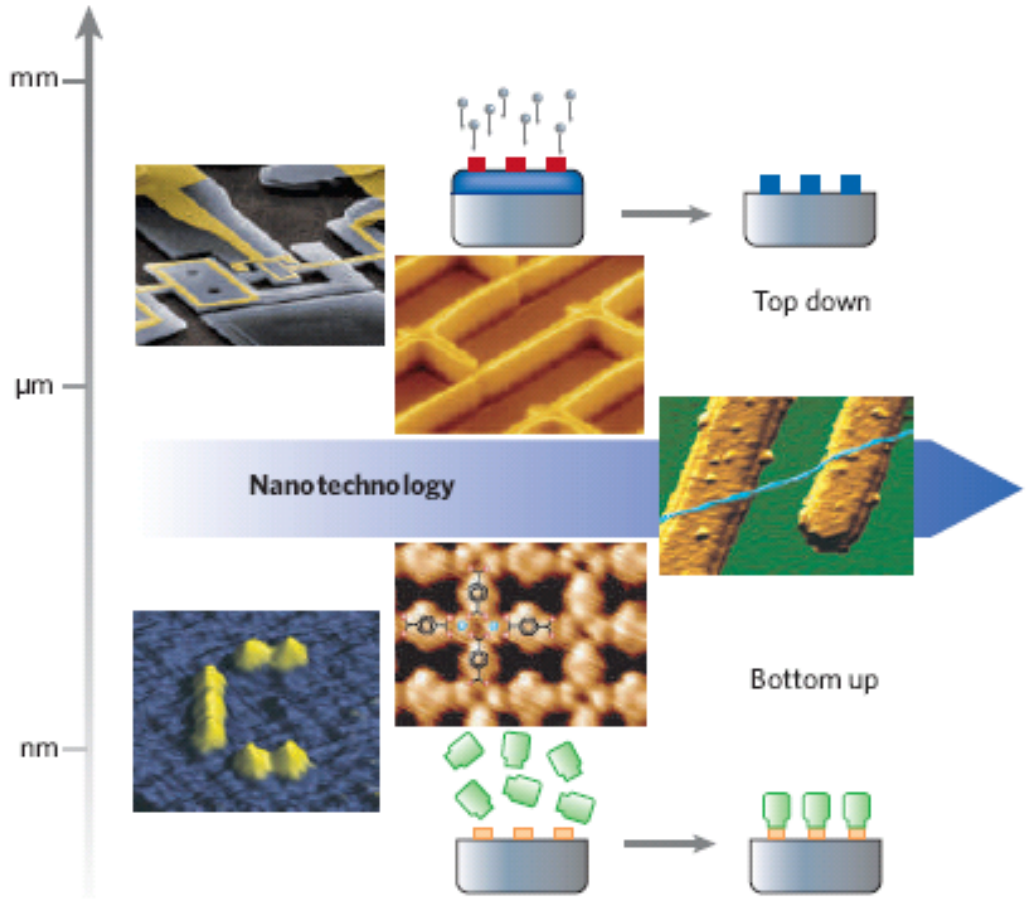

Figure 1.2 Two approaches to control matter at the nanoscale. For top-down fabrication, methods such as lithography, writing or stamping are used to define the desired features. The bottom-up techniques make use of self-processes or ordering of supramolecular or solid-state architectures from the atomic to the mesosopic scale. Shown (clockwise from top) are an electron microscopy image of a nanomechanical electrometer obtained by electron-beam lithography [41b], patterned films of carbon nanotubes obtained by microcontact printing and catalytic growth, a single carbon nanotube connecting two electrodes [41c], a regular metal-organic nanoporous network integrating iron atoms and functional molecules, and seven carbon monoxide molecules forming the letter 'C' positioned with the tip of a scanning tunnelling microscope (image taken from http://www.physics.ubc.ca/~stm/).

Self-assembly is an efficient and low-cost tool for the "bottom-up" fabrication of nanostructures. The key idea of self-assembly is that nanostructures can be spontaneously formed taking advantage of some energetic, kinetic and geometric effects in materials growth processes. It is generally a parallel fabrication process as many nanostructures are produced simultaneously. Those factors make self-assembly one of the most promising methods for nanostructure and nanodevice fabrication. In the rest of this section, the basic concepts in materials growth will be briefly reviewed first, followed with the introduction of some self-assembly techniques for fabricating nanostructures.

1.2.1 Basic concepts in materials growth

Self-assembly of nanostructures on well defined surfaces is essentially based on growth phenomena and governed by the competition between kinetics and thermodynamics. The primary atomic or molecular processes that occur during material growth on substrate surfaces are shown schematically in Figure 1.3 [46, 47]. Atoms or molecules are delivered to the substrate and a large fraction of these species adsorb on the surface. Once adsorbed, there are three things that may happen to the adatom. It can form a strong bond to the surface where it is trapped, diffuses on the terraces to find an energetically preferred location prior to being trapped, or evaporate away from the surface (desorption). The adatoms diffuse on

the surface until they (1) desorb from the surface; (2) find another adatom and nucleate into an island; (3) attach to an existing island; (4) are trapped at defect sites; or (4) diffuse into the surface. The last two events are often considered relatively rare but are important in nanostructure fabrication. For example the adsorption of atoms or cluster at step edges can yield quasi-nanowires or clusters.

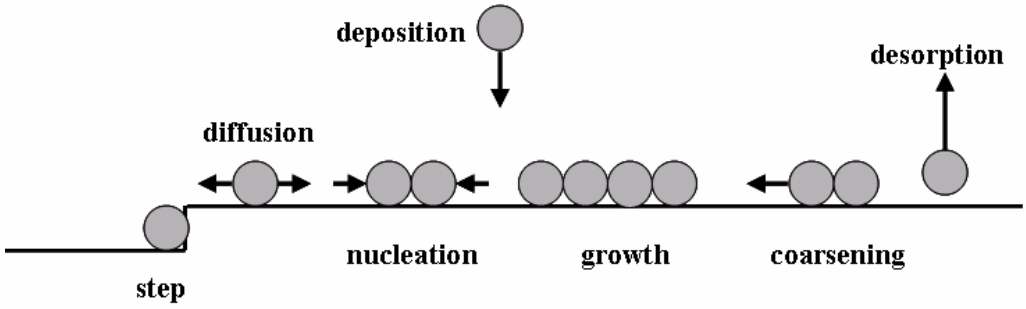

Figure 1.3 Schematic illustrations of atomic processes in crystal growth from vapor.

The evolution of island formation can be visualized as a process with three different growth regimes. Initially, there is high concentration of adatoms or monomers diffusing on the surface, resulting in a high probability of island nucleation. This is the nucleation regime, where the density of islands on the surface increases with coverage. The density continues to increase until the probability of a diffusing adatom finding an island is much higher than the

probability to find another adatom. The number of nucleation events is substantially reduced as the adatom diffusion length becomes large relative to the average island spacing. Thus the majority of events occurring are adatoms attaching to the existing islands, hence defining the aggregation regime. As further growth in the aggregation regime, the island density remains relatively constant while the islands continue to grow in size. Eventually, the islands will begin to merge with each other and enter into coalescence regime, which is signified by a decrease in the island density with increasing coverage.

In the case of heteroepitaxy where the substrate and deposited materials are different, there are three different growth modes, depending on the surface and interfacial energy as well as lattice mismatch between the deposited materials and substrate as indicated in Figure 1.4. When the lattice mismatch is small and the interface binding is strong, the film grows in a layer-by-layer (Frank-Van der Merwe) mode. If the interface bonding is weak ($\gamma_{int} \geq \gamma_s - \gamma_f$, γ_f is surface energy of the film), the deposited material grows in 3D islanding (Volmer-Weber) mode. If the interface binding is strong but the lattice mismatch is relatively large, the film will grow in the layer-by-layer mode initially, followed by 3D-islanding. This process is known as the Stranski-Krastanov (S-K) mode. The initial wetting layer grows in the lattice constant of substrate, so it is elastically strained. The strain energy increases with film thickness. At certain point the 3D islands form as a

way to release the strain energy. As the film becomes even thicker, eventually the strain energy is released by forming misfit dislocations. As will be seen below, the Volmer-Weber and S-K modes are crucial for the self-assembled growth of an array of nanoparticles or quantum dots on substrate.

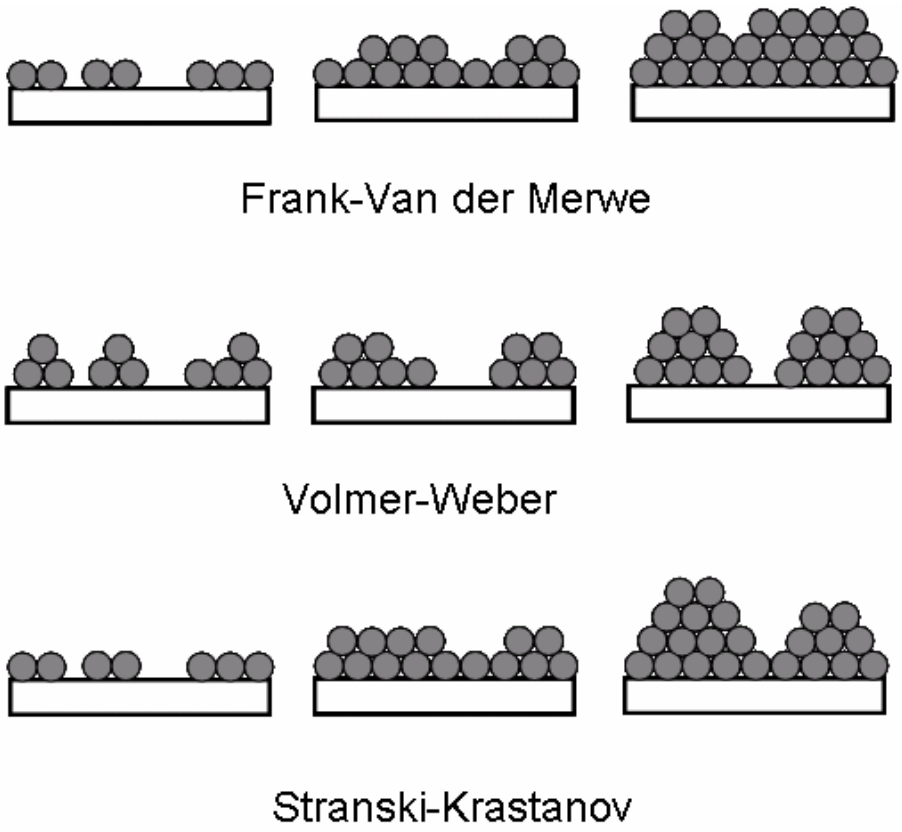

Figure 1.4 Schematic illustrations of three growth modes in heteroepitaxy

1.2.2 Self-assembly of nanostructures on surface

As mentioned in the introduction, self-assembly approaches to fabricate nanostructures have the advantage that the structures are formed in the growth environment and no processing is needed. In recent years, a great variety of self-assembly methods have been extensively explored, aiming at fabricating well-ordered nanostructure arrays with controlled shape, composition and high spatial density over macroscopic areas. In the following, we will discuss the main self-assembly methods which are frequently used to fabricate nanostructures on surfaces.

Self-assembly based on Stranski-Krastanow and Volmer-Weber growth modes

As mentioned above, the growth of islands is accompanied in both Stranski-Krastanow (S-K) and Volmer-Weber (V-W) mode, depending on the lattice mismatch and surface energy. Accordingly, the self-assembly of QDs, nanocrystals and clusters can be routinely obtained for several heteroepitaxial systems [1, 39, 43]. Elegant examples based on S-K growth mode include Ge QDs on Si (4% lattice mismatch) [24, 48, 49] and InAs QD on GaAs (7% lattice mismatch) [50, 51]. The two types of QDs are produced with defect-free but strained islands forming spontaneously on top of a thin wetting layer during the

lattice-mismatched heteroepitaxial growth. Such QDs were often found to have a narrow size distribution and to be arranged in a regular array, which have promising application in the fields of nanoelectronics and quantum dot lasers. Figure 1.5 shows STM images of Ge nanocrystals with rectangular hut and square pyramid shape on Si(001) obtained in our lab.

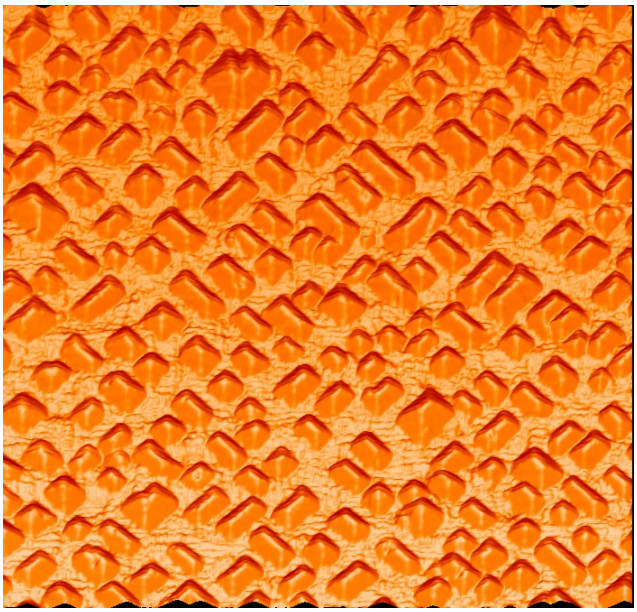

Figure 1.5 STM image of Ge on Si(001): rectangular hut and square pyramid Ge nanocrystals can be clearly observed.

V-W growth has also been widely exploited to fabricate nanoscale clusters. As this growth mode requires a low free energy/chemically inert surface, common

substrates include graphite, passivated Si/GaAs and metal oxides. Graphite is a prototypical substrate with low surface energy. Lots of works have been focused on the interaction of a range of metals and semiconductors (Cu, Ag, Au, Al, Co, Fe, Si and Ge) [52-56] with graphite, observing the formation of nearly free-standing nanoparticles or clusters. We have grown Ge clusters on graphite in our group. The Ge atoms have high mobility on the inert graphite and form Ge clusters with narrow size distribution. The formation of MnSb nanoparticle chains on graphite will be discussed in Chapter 3. Passivated semiconductor substrates such as Si and GaAs have been employed to create inert substrates for the V-W growth of nanoscale clusters.

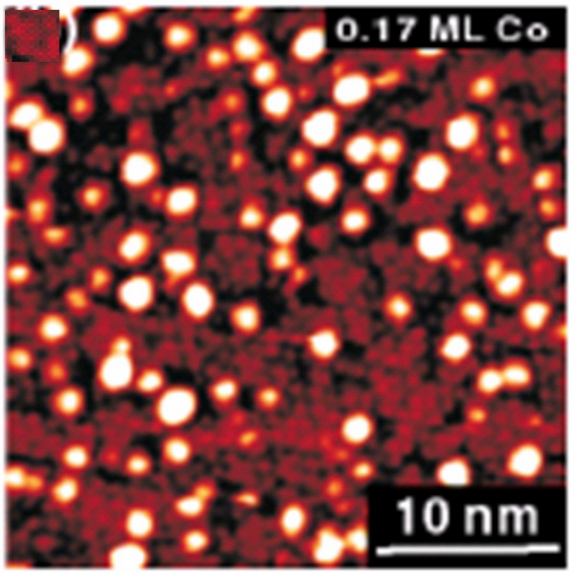

Figure 1.6 STM images of Co nanoclusters grown on the Si_3N_4 (0001) ultrathin film at room temperature with 0.17 ML of Co deposition [63].

Hydrogen passivated Si(001) surface have been commonly used for growth of a range of metal nanoparticles(Ag, Co, Au and Fe) [57, 58]. Researchers in Weaver's group have reported a novel method of forming nanocrystals on Si(111)-(7 × 7) which involves the use of buffer layers of Xe [59, 60]. As will be introduced in Chapter 5, Si(111) covered with a thin layer SiN_x (x ~ 4/3) buffer layer provide a good substrate to self-assembly nanoparticles and cluster. It is chemically stable and quite inert, acting as a block layer against interdiffussion reaction which is a common problem for metal cluster grown on Si(111) [61-63]. Figure 1.6 shows STM image of Co nanoclusters formed on Si_3N_4(0001). The Co clusters show narrow size distribution, due to the self-limiting size distribution originating from a quantum size effect, manifested by local energy minima in the electronic shell structure of Co quantum dots. In this work, we have fabricated MnSb nanoparticles with controllable diameters on Si(111) covered with a thin layer Si_3N_4. As shown later the Si_3N_4 provides a good buffer layer for the growth of metal or compound nanostructures. The principal motivation for the study of metal particles on metal oxide substrates relates to their use in heterogeneous catalysis, high density data storage and sensor. Commonly used oxide substrates include MgO [64, 65] , metal-supported Al_2O_3 [21, 66] and $SrTiO_3$ [67-69]. Bäumer and Freund [21] have reviewed works in this field, concentrating on growth of a range of metals (Ag, Rh, V, Pd, Co, Pt) on metal-supported thin

alumina films. Figure 1.7 shows STM image of well ordered Pd nanocrystals formed on $SrTiO_3$ (4 × 2) substrate [68]. By controlling the temperature during the deposition process, Pd nanocrystals with hexagon and pyramid shape could be selectively assembled.

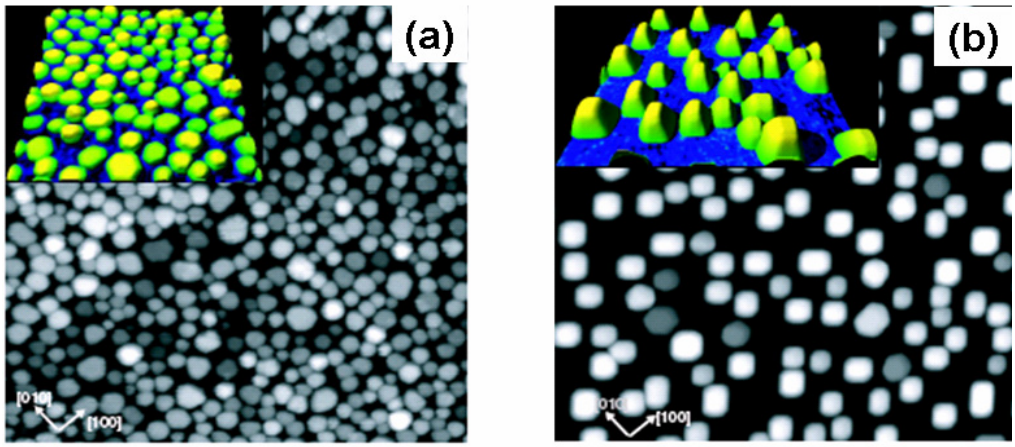

Figure 1.7 Pd nanocrystals formed on $SrTiO_3$ substrate [68]. (a) Hexagonal nanocrystals are formed following Pd deposition onto a room temperature $SrTiO_3$ (4 × 2) substrate followed by a 650 ^oC anneal as shown in the STM image (140 ×140 nm^2); (b) Pd deposited onto a 460 ^oC $SrTiO_3$ (4 × 2) substrate followed by a 650 ^oC anneal gives rise to truncated pyramid shaped Pd nanocrystals as shown in the STM image (140 ×140 nm^2).

Self-assembly of nanostructures on nanotemplate

Another promising route of self-assembly is to utilize well-defined nanotemplates to guide the formation of nanostructures. Such nanotemplates are naturally or artificially patterned at the nanoscale on surface. The most easily produced and simplest nanotemplates are the superstructure arising from reconstructions on metal or semiconductor surfaces. The well-known Au(111)-*(*22 ×√3*)* reconstruction due to strain relief takes the form of a 'herring-bone' pattern. The elbows of the herring-bone pattern provide preferential nucleation sites for materials with a large lattice mismatch, like Co [70]. Deposition of sub-monolayer of Co on Au (111)-(22 × √3) produces an array of two-layer-high Co islands [74]. The islands are nucleated at the 'elbows' of the herring-bone reconstruction. Thus, the Au(111) substrate not only promotes Co island formation, but also acts as a template for the lateral positions of the islands. Recently, the formation of highly ordered superlattice comprising magic nanoclusters have been achieved with group-III metal (Al, In, Ga) and sodium (Na) on Si(111)-7×7 [71-74]. Take the growth of Al nanoclusters on Si(111)-7×7 for example [74], the Al prefer to occupy the faulted half unit-cells of Si(111)-7×7 to form perfectly ordered "magic" sized nanocluster arrays. The Al nanocluster arrays provided templates for self-assembly magnetic Co nanoparticles [33].

1.3 Magnetic nanostructure and MnSb

1.3.1 Magnetic nanostructure

Since the early days of condensed matter physics, the study of magnetic materials has played a central role in establishing the fundamental principles and concepts of the field. Magnetic materials have a diverse range of applications in modern society such as data storage media, random access memory in computer, automotive sensors and electric motors [75, 76]. Research on magnetic materials has driven the sample physical size towards smaller dimensions for device miniaturization [77]. In the past decade, we have been witnessing great advances in the understanding of the magnetism and spin-dependent transport in various magnetic nanostructures, and their related applications [78-80]. As mention in Section 1.1, nanostructures usually possess unique properties due to the low-dimensional quantum confinement effect. When the magnetic materials are reduced to nanoscale, they exhibit a number of outstanding physical properties such as giant magnetoresistance (GMR), superparamagnetism, enhanced magnetic moment, as compared to the corresponding bulk values [78, 79, 81]. Due to these outstanding physical properties, magnetic nanostructures are bringing revolutionary changes in device applications, especially in high-density data storage and spintronic devices. For example, the GMR effect in magnetic ultrathin multilayer structures has been exploited to increase the capacity of hard discs by

over a factor of a hundred in a small number of years and non-volatile magnetic random access memories (MRAM) are starting to be utilized in computer and communication devices [82-84]. Generally, magnetic nanostructure can be classified into thin film or multilayer structures (2D), magnetic nanowire or nanorods (1D) and magnetic nanoparticles or quantum dots (0D) [83], like nanostructures mentioned at the beginning of this Chapter.

Magnetic multilayer

Magnetic multilayer structures refer to utrathin (a few atomic layers) alternating layers of magnetic materials and non-magnetic materials [82]. For example, in a typical multilayer structure for GMR effect, two ferromagnetic layers are separated by a very thin (about 1 nm) non-ferromagnetic spacer (e.g. Fe/Cr/Fe) [85], as sketched in Figure 1.8. A huge magnetoresistance (MR) can be observed due to the spin-dependent transport in the layered structures. If the two ferromagnetic layers are seperated by a thin layer (1 nm) of insulator, such as Al_2O_3, a magnetic tunnel junction (MTJ) can be fabricated which can be used as the storage cells for MRAM [82]. Here, we should emphasize that the growth of magnetic thin films on semiconductor is of great technological importance, because magnetism can be integrated into the semiconductor electronics which have promising application in spintronics. For example, ferromagnetic MnAs thin

film has been fabricated on GaAs [86]. Spin-polarized electrons can be injected from the ferromagnetic MnAs to the GaAs. In this work, we also study the deposition of ferromagnetic MnSb on the Si-based substrate so that Si-based spintronic structures become possible.

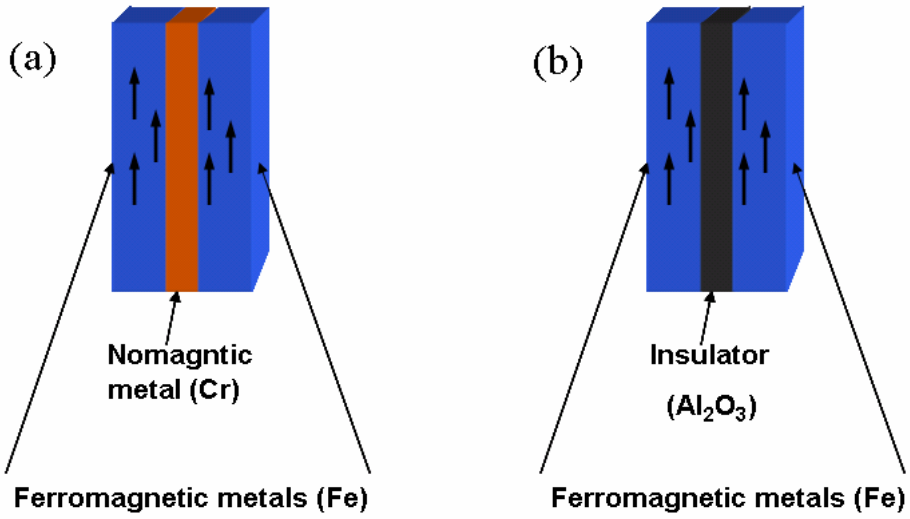

Figure 1.8 Schematic drawing of (a) Ferromagnetic/ Nonmagetic/ Ferromagnetic trilayer for GMR; (b) A MTJ trilayer structure formed by two ferromagnetic metals.

Magnetic nanoparticles

Considerable process has been made as well in the field of magnetic nanoparticle systems [80, 87-89]. Ordered magnetic nanoparticle arrays have the

capability of reaching ultra high density storage [90-91]. Due to the finite size and change of lattice structure in the magnetic nanoparticles, some of the magnetic properties such as magnetic moment, MR and magnetocrystalline anisotropy are going to be remarkably altered. Superparamagentism, enhanced magnetic moment and GMR effects have been observed in magnetic nanoparticle systems [8, 33, 92]. For example, superparamagentic bahavor was frequently observed for magnetic nanoparticles (e.g. Co nanoparticle on Au(111) [93]) with very small sizes (1-10 nm), because the magnet volume is so small that thermal energy (k_BT) can trigger the transition from one magnetization state to others. The effect of supermagnetism is that the nanoparticles have a large moment with high saturation magnetization but a non-hysteretic M-H curve with zero remanence and coercivity. In data storage applications, the superparamagnetism sets limit on the size of nanoparticles which limit the capacity of magnetic recording media.

A variety of magnetic nanoparticles supported on surfaces have been fabricated by self-assembly method. Ferromagnetic metal nanoparticales with narrow size distribution such as Fe, Co, Ni and FePt have been formed on different substrates [33, 36, 94-105]. The most extensively studied system is Co clusters grown on Au(111)-(22 × √3), as mentioned above [70, 93, 104, 105]. Ferromagnetic compounds such as MnSb and MnAs quantum dots have been self-assembled on sulfur-passivated GaAs which had a low surface energy due to the

passivation [38, 93]. A huge MR effect was observed, and hence made them promising candidate for magnetoresistive switch. Another method to prepare magnetic nanoparticles is to anneal diluted magnetic semiconductor, like $Ga_{1-x}Mn_xAs$ [106-108]. By controlling the x value and annealing temperature, MnAs cluster with controllable diameter and concentration have been fabrication embedded in the GaAs. The granular GaAs:MnAs films exhibit GMR and giant magneto-optical effects.

1.3.2 Magnanese antimonide

Manganese-based compounds, such as maganese pnictides，chalcogenides and their alloys, have received considerable attention because of their interesting magnetic and magneto-optical properties. Especially, the ferromagnetic thin films, such as CuAu-type MnGa, MnAl and NiAs-type MnAs and MnSb [109-114], have been successfully grown on GaAs and Si by molecular beam epitaxy, offering attractive possibilities of fabricating new hybrid devices combining magnetic metal layers with semiconductor substrates. Among various ferromagnetic materials, α-MnSb possess several properties highly desirable for device application. It has a high Curie temperature of 317°C and a high saturate magnetization [93]. α-MnSb has a hexagonal NiAs-type crystal structure, with lattice constants of a = 4.128 Å and c = 5.789 Å, as sketched in Figure 1.9. It has

strong magnetocrystalline anisotropy and the easy magnetization direction parallels to the (0001) plane. Furthermore, MnSb is highly spin polarized, especially the zincblende-phase MnSb which is nearly half-metallic [115,116]. A large magnetic Kerr rotation was reported from the near infrared through the visible wavelength region [117]. The above-mentioned properties make MnSb a very promising material in magneto-optical application.

MnSb films and nanoparticles have been grown on semiconductors such as GaAs [118-122] and Si [123-125]. The epitaxial relationships, interfacial structure and morphologies, magnetic properties have been extensively studied. It has been demonstrated that MnSb epitaxial layers grown on GaAs(001) and GaAs(111) had orientation of MnSb(1 $\bar{1}$ 01) and MnSb(0001), respectively [121, 122]. MnSb(0001) films have been obtained on Si(111) at a substrate of 300^{o}C [125]. Ferromagntic properties were observed at room temperature. However, the surface structure and chemical states of the grown MnSb have not been examined carefully. These factors are of crucial importance for better understanding of the growth process and magnetic properties of MnSb. As such, in this work, we utilized *in situ* scanning tunneling microscopy (STM) to analyze the surface structure and morphology of MnSb films and nanoparticles prepared on different substrates. The chemical and magnetic properties of MnSb are studied with other characterization techniques.

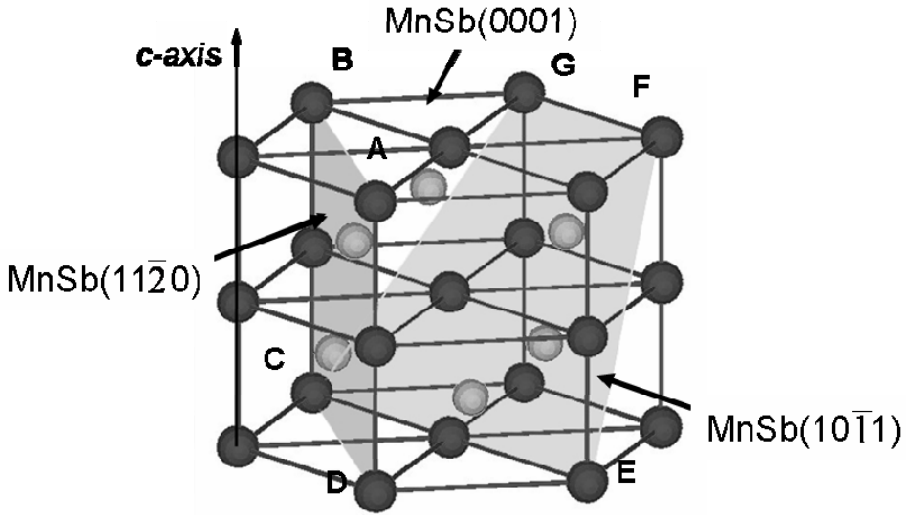

Figure 1.9 Crystal structure of MnSb. The *c*-axis is indicated by the arrow, and MnSb $(11\bar{2}0)$ and $(10\bar{1}1)$ planes are indicated by ABCD and CEFG, respectively.

1.4 Synopsis of Chapters

Chapter 2 of the thesis provides an overview of the working principles of characterization techniques used, including surface analytical probes (STM, AES/XPS), structural characterization techniques (XRD, TEM) and magnetic measurement tools (VSM, SQUID). In Chapter 3, the surface morphologies of MnSb thin films and nanoparticles on HOPG are studied with STM. Different MnSb superstructures will be revealed by the atomic resolution images, which will provide useful information to guide our following epitaxial preparation of

MnSb compounds on Si-based substrate. The growth of MnSb compounds on Si(111) substrate is presented in Chapter 4 where the influence of substrate temperature on MnSb surface morphology and interfacial structures is studied. Finally, in Chapter 6, we will present the self-assembly of MnSb nanoparticle with controllable size on Si(111) with a SiN buffer layer. The magnetic properties correlated to the size of nanoparticles will be studied and explained.

Reference:

[1] H. S. Nalwa, *Handbook of nanostructured materials and nanotechnology*, Academic press New York (2000).

[2] G. M. Whitesides, B. Grzybowski, *Science* **295**, 2418 (2002).

[3] A. Thiaville, J. Miltat, *Science* **284**, 1939 (1999).

[4] S. Luryi, J. Xu, and A. Zaslavsky, *Future trends in microelectronics: The nano millennium, Wiley-interscience,* Now York (2002).

[5] P. Moriarty, *Rep. Prog. Phys.* **64**, 297 (2001).

[6] International Technology Roadmap for Semiconductors (ITRS) 2006 Website *http://www.itrs.net/*

[7] H. K. Wickramasinghe, *Acta Mater.* **48**, 347 (2000).

[8] P. Gambardella, *et al. Nature* **416**, 301 (2002).

[9] C. B. Murray, C.R. Kagan，M. G. Bawendi, *Annu. Rev. Mater. Sci.* **30**, 545 (2000).

[10] J. M. Krans, J. M. van Rutenbeek, V. V. Fisun, I. K. Yanson, and L. J. Jongh, *Nature* **375**, 767 (1995).

[11] G. Markovich, C. P. Collier, S. E. Henrichs, F. Remacle, R. D. Levine, and J.R. Heath, *Acc. Chem. Res.* **32**, 415 (1999).

[12] K. Barnham, D. D Vvedensky (eds.), *Low-dimensional semiconductor structures: Fundamentals and device applications,* Cambridge University

Press, New York (2001).

[13] S. Ciraci, S. Dag, T. Yildirim, O. Gülseren, R.T. Senger, *J. Phys.: Condens. Matter* **16**, R901 (2004).

[14] Ph. Avouris, *Chem. Phys.* **281**, 429 (2002).

[15] Y. Cui, C. M. Lieber, *Science* **291**, 851 (2001).

[16] Y. Wu, R. Fan, P. Yang, *Nano Lett.* **2**, 83 (2002).

[17] X. Duan, C.M. Lieber, *J. Am. Chem. Soc.* **122**, 188 (2000).

[18] G. T. Wang *et al. Nanotechnology* **23,** 5773 (2006).

[19] Z.W. Pan, Z. R. Dai, *Science* **291**, 1947 (2001).

[20] Y. Xia, P. Yang, Y. Sun, Y. Wu, B. Mayers, B. Gates, Y. Yin, F. Kim, H. Yan, *Adv. Mater.* **15**, 353 (2003).

[21] M. Baumer and H. J. Freund, *Prog. Surf. Sci.* **61**, 127 (1999).

[22] C. Binns, *Surf. Sci. Rep.* **44**, 1 (2001).

[23] Christian Teichert, *Phys. Rep.* **365**, 335 (2002).

[24] Y. W. Mo, D. E. Savage, B. S. Swartzentruber, M. G. Lagally, *Phys. Rev. Lett.* **65**, 1020 (1990).

[25] R. S. Williams, G. Medeiros-Ribeiro, T. I. Kamins, D. A. A. Ohlberg, *Annu. Rev. Phys. Chem.* **51**, 527 (2000).

[26] C. Adelmann, B. Daudin, R. A. Oliver, G. A. D. Briggs, and R. E. Rudd，*Phys. Rev. B* **70,** 125427 (2004).

[27] D. Fuster, B. Alén, L. González, Y. González, J. Martínez-Pastor, M. U. González, J. M. García, *Nanotechnology* **18,** 035604 (2007)

[28] D. A. Tenne, V. A. Haisler, A. I. Toropov, A. K. Bakarov, A. K. Gutakovsky, D. R. Zahn, and A. P. Shebanin ,*Phys. Rev. B* **61,** 13785 (2000).

[29] X. Peng, L. Manna, W. Yang, J. Wickham, E. Scher, A. Kadavanich, A. P. Alivisatos, *Nature* **404**, 59 (2000).

[30] T. Schmidt, E. Roventa, T. Clausen, J. I. Flege, G. Alexe, S. Bernstorff, C. Kübel, A. Rosenauer, D. Hommel, and J. Falta, *Phys. Rev. B* **72,** 195334 (2005).

[31] F. Rosei, *J. Phys.: Condens. Matter* **16**, S1373 (2004).

[32] F. Komori, K.D. Lee, K. Nakatsuji, T. Iimori, Y.Q. Cai, *Phys. Rev. B* **63**, 214420 (2001).

[33] M. H. Pan *et al. Nano. Lett.* **5**, 87 (2005).

[34] F. J. Himpsel *et al*. *Advances in Physics*, **47**, 511 (1998).

[35] H. Zhou, J. Narayan, *Journal of Nanoparticle Research* **8,** 595 (2006).

[36] S. H. Sun, C. B. Murray, D. Weller, L. Folks and A. Moser, *Science* **281**,1989 (2000).

[37] K. Y. Wang, M. Sawicki, K. W. Edmonds, R. P. Campion, A.W. Rushforth, A. A. Freeman, C. T. Foxon, B. L. Gallagher, and T. Dietl, *Appl. Phys. Lett.* **88**, 022510 (2006).

[38] H. Akinaga, M. Mizuguchi, K. Ono, and M. Oshima, *Appl. Phys. Lett.* **76**, 2600 (2000).

[39] G. Timp (ed.), *Nanotechnology*, Springer, New York (1999).

[40] Y. N. Xia, J. A. Rogers, K. E. Paul, and G. M. Whitesides, *Chem. Rev.* **99,** 1823 (1999).

[41] a, J. V. Barth, G. Costantini and K. Kern, *Nature* **437**, 679 (2005); b, A. N. Cleland and M. L. Roukes, *Nature* **392**, 160 (1998); c, S. J.Tans, M. H. Devoret, R. J. A.Groeneveld, and C. Dekker, *Nature* **394**, 761(1998).

[42] T. Ito, S. Okazaki, *Nature* **406**, 1027 (2000).

[43] S. Franchi, G. Trevisi, L. Seravalli, P. Frigeri, , *Prog. Cryst. Growth Charact. Mater.* **47**, 166 (2003).

[44] R. F. Service, *Science* **293**, 782 (2001).

[45] B. A. Joyce, D. D. Vvedensky, *Mater. Sci. Eng.* ***R*** **46**, 127 (2004).

[46] F. Bechstedt, *Principles of surface physics*, Springer, Berlin (2003).

[47] H. Lüth, *Solid surfaces, interface and thin films*, Springer, Berlin (2001).

[48] G. Costantini, *et al*., *Appl. Phys. Lett.* **85**, 5673 (2004).

[49] I. Daruka, J. Tersoff, A. L. Barabasi, *Phys. Rev. Lett.* **82,** 2753 (1999).

[50] J. M. Moison *et al.*, *Appl. Phys. Lett.* **64**, 196 (1994).

[51] R. Heitz *et al.*, *Phys. Rev. Lett.* **78**, 4071 (1997).

[52] E. Ganz, K. Sattler and J. Clarke, *Phys. Rev. Lett.* **60,** 1856(1988).

[53] E. Ganz, K. Sattler and J. Clarke, *Surf. Sci.* **219,** 33(1989).

[54] P. Sheier, B. Marsen, M. Lonfat, W. D. Shneider and K. Sattler, *Surf. Sci.* **458** 113 (2000).

[55] I. Barke and H. Hövel, *Phys. Rev. Lett.* **90**, 166801 (2003).

[56] H. Hövel and I. Barke, *Prog. Surf. Sci.* **81**, 53 (2006).

[57] M. J. Butcher, *et al., Phys. Rev. Lett.* **83,** 3478 (1999).

[58] G. Palasantza, B. Ilge, J. DeNijs and L. J. Geerligs *J. Appl. Phys.* **85,** 1907 (1999).

[59] L. Huang, S. J. Chey and J. H. Weaver, *Phys. Rev. Lett.* **80,** 4095 (1998)

[60] S. J. Chey, L. Huang and J. H. Weaver, *Phys. Rev.* B **59,** 16 033 (1999).

[61] X.-S. Wang, G. Zhai, J. Yang, L. Wang, Y. Hu, Z. Li, J.C. Tang, X. Wang, K.K. Fung, and N. Cue, *Surf. Sci.* **494**, 83 (2001).

[62] L. Wang, Y. Hu, Z. Li, J.-C. Tang, and X.-S. Wang, *Nanotechnology* **13**, 714 (2002).

[63] S. Gwo, C.-P. Chou, C.-L. Wu, Y.-J. Ye, S.-J. Tsai, W.-C. Lin, and M.-T. Lin,

Phys. Rev. Lett. **90**, 185506 (2003).

[64] S. Schintke *et al.*, *Phys. Rev. Lett.* **87**, 276 801(2001).

[65] W. D. Schneider *Surf. Sci.* **514**, 74 (2002)

[66] R. M. Jaeger, H. Kuhlenbeck and H. J. Freud, *Surf. Sci.* **259,** 235 (1991).

[67] M. R. Castell, *Surf. Sci.* **505**, 1 (2002).

[68] F. Silly and M. R. Castell, *Phys. Rev. Lett.* **94,** 046103 (2005).

[69] F. Silly and M. R. Castell, *Phys. Rev. Lett.* **96,** 086104 (2006).

[70] C. Tolkes, P. Zeppenfeld, M. A. Krzyowski, R. David and G. Comsa, *Phys. Rev. B* **55,** 13 932 (1997).

[71] K. H. Wu, *et al., Phys. Rev. Lett.* **91,** 126101 (2003).

[72] J. L. Li, *et al., Phys. Rev. Lett.* **88,** 066101 (2003).

[73] M. Y. Lai and Y. L. Wang, *Phys. Rev. B.* **64,** 241404 (2001).

[74] V.G. Kotlyar, *et al., Phys. Rev. B.* **66**, 165401 (2002).

[75] C. Kittel, *Introduction to Solid State Physics*, Wiley, New York (1996)

[76] E. du T. de Lacheisserie, D. Gignoux and M. Shlernker, *Magnetism I-fundamentals and II-materials and application*, Kluwer Norwell (2002).

[77] A. Moser *et al*., *J. Phys. D: Appl. Phys.* **35**, R157 (2002).

[78] R. Skmoski, Nanomagnetics, *J. Phys.: Condens. Matter* **15**, R841 (2003).

[79] J. I. Martín, J. Nogués, K. Liu, J. L. Vicent, I. K. Schuller, *J. Magn. Magn. Mater.* **256**, 449 (2003).

[80] I. Žutić, J. Fabian, S. Das Sarma, *Rev. Mod. Phys.* **76**, 323 (2004).

[81] F.J. Himpsel, J.E. Ortega, G.J. Mankey, R.F. Willis, *Adv. Phys.* **47**, 511 (1998).

[82] U. Hartmann (ed.), *Magnetic multilayers and giant magnetoresistance: fundamentals and industrial applications*, Springer, New York (1999).

[83] E. Burstein, M. L. Cohen, D. L. Mills and P. J. Stiles, *Nanomagnetism*, Elsevier, Amsterdam (2006).

[84] S. Parkin *et al*., *Proc. IEEE* **91**, 661 (2003).

[85] M. N. Baibich, J. M. Broto, A. Fert, F. Nguyen Van Dau, F. Petroff, P. Eitenne, G. Creuzet, A. Friederich, and J. Chazelas, *Phys. Rev. Lett.* **61**, 2472 (1988).

[86] A. K. Das, C. Pampuch, A. Ney, T. Hesjedal, L. Däweritz, R. Koch, and K.H. Ploog, *Phys. Rev. Lett.* **91**, 087203 (2003).

[87] G. A. Prinz, *Science* **250**, 1092 (1990).

[88] J. Shen, J. Kirschner, *Surf. Sci.* **500**, 300 (2002).

[89] S. Sun, *et al., Science* **287** 1989 (2000).

[90] F. J. Himpsel, *et al,. Adv. Phys.* **47** 511 (1998).

[91] S. Rusponi, *et al., Nature Mater.* **300** 1130 (2003).

[92] H. Akinaga, M. Mizuguchi, K. Ono, and M. Oshima, *Appl. Phys. Lett.* **76**, 2600 (2000).

[93] H. Takeshita, Y. Suzuki, H.Akinaga, W. Mizutani, K. Ando, T. Katayama, A.

Itoh and K. Tanaka *J. Magn. Magn. Mater.* **165**, 38 (1997).

[94] Z. Gai, B. Wu, J. P. Pierce, G. A. Farnan, D. Shu, M. Wang, Z. Zhang, and J. Shen, *Phys. Rev. Lett.* **83,** 235502 (2002).

[95] P. Ohresser, N. B. Brookes, S. Padovani, F. Scheurer, and H. Bulou, *Phys. Rev. B* **64**, 104429 (2001).

[96] F. Silly and M.R. Castell, *Appl. Phy.s Lett.* **87**, 063106 (2005).

[97] W. C. Lin, C. C. Kuo, M. F. Luo, K. J. Song and M. T. Lin, *Appl. Phys. Lett.* **86**, 043105 (2005).

[98] F. Silly and M. R. Castell, *Appl. Phys. Lett.* **87**, 053106 (2005).

[99] V. Podgursky, I. Costina, R. Franchy, *Surf. Sci.* **529**, 419 (2003).

[100] A. Kida, H. Kajiyama, S. Heike, T. Hashizume, and K. Koike, *Appl. Phys. Lett.* **75**, 540 (1999).

[101] Y. Shiratsuchi, M. Yamamoto, Y. Endo, D. Q. Li, and S. D. Bader, *J. Appl. Phys.* **94**, 7675 (2003).

[102] H. A. Dürr, S. S. Dhesi, and E. Dudzik, D. Knabben, G. van der Laan, J. B. Goedkoop, and F. U. Hillebrecht, *Phys. Rev. B* **59**, R701 (1999).

[103] J. Xu, M. A. Howson, B. J. Hickey, D. Greig, E. Kolb, P. Veillet and N. Wiser, *Phys. Rev. B* **55**, 416 (1997).

[104] T. Koide, H. Miyauchi, J. Okamoto, T. Shidara, A. Fujimori, H. Fukutani, K. Amemiya, H. Takeshita, S. Yuasa, T. Katayama, and Y. Suzuki, *Phys. Rev.*

Lett. **87**, 257 201(1988).

[105] J. Bansmann, S. H. Baker, C. Binns, J. A. Blackman, J.-P. Bucher, J. Dorantes-Dávila, V. Dupuis, L. Favre, D. Kechrakos, A. Kleibert, K. H. Meiwes-Broer, G.M. Pastor, A. Perez, O. Toulemonde, K. N. Trohidou, J. Tuaillon and Y. Xie, *Surf. Sci. Rep.* **56**, 189 (2005).

[106] H. Akinaga, S. Miyanishi, K. Tanaka, W. Van Roy, and K. Onodera, *Appl. Phys. Lett.* **76**, 97 (2000).

[107] M. Yokoyama, H. Yamaguchi, T. Ogawa and M. Tanaka, *J. Appl. Phys.* **97**, 10D317 (2005).

[108] K.Y. Wang, M. Sawicki, K.W. Edmonds, R.P. Campion, A.W. Rushforth, A.A. Freeman, C.T. Foxon, B.L. Gallagher, and T. Dietl, *Appl. Phys. Lett.* **88**, 022510 (2006).

[109] K.M. Krishnan, *Appl. Phys. Lett.* **61**, 2365 (1992).

[110] A. Ouerghi, M. Marangolo, M. Eddrief, S. Guyard, V.H. Etgens, and Y. Garreau, *Phys. Rev. B* **68**, 115309 (2003).

[111] A. M. Nazmul, A.G. Banshchikov, H. Shimizu, and M. Tanaka, *J. Cryst. Growth* **227**, 874 (2001).

[112] M. Tanaka, *Semicond. Sci. Technol.* **17**, 327 (2002).

[113] A. K. Das, C. Pampuch, A. Ney, T. Hesjedal, L. Däwerits, R. Koch, and K. H. Ploog, *Phys. Rev. Lett.* **91**, 087203 (2003)

[114] H. Fujioka, Y. Noguchi, T. Ikeda, H. Katada, K. Ono, M. Oshima, *J. Cryst. Growth* **229**, 537 (2001).

[115] A. Continenza, S. Picozzi, W. T. Geng, and A. J. Freeman*, Phys. Rev. B **64***, 085204 (2001).

[116] S. J. Jenkins, *Phys. Rev. B* **70**, 245401 (2004).

[117] M. Takahashi, H. Shoji, Y. Hozumi, and T. Wakiyama, *J. Magn. Magn. Mater.* **131**, 67 (1994).

[118] H. Akinaga, S. Miyanishi, W. Van Roy, J. De Boeck and G. Borghs, *Appl. Phys. Lett.* **70**, 2472 (1998).

[119] B. L. Low, C. K. Ong, G. C. Han, H. Gong, T. Y. F. Liew H. Tatsuoka, H. Kuwabara, and Z. Yang, *J. Appl. Phys.* **84**, 973 (1998).

[120] B. L. Low, C. K. Ong, J. Lin, A. C. H. Huan, H. Gong, and T. Y. F. Liew, *J. Appl. Phys.* **85**, 7340 (1999).

[121] S. X. Liu, S. M. Bedair and N. A. El-Masry, *Mater. Lett.* **42**, 121 (2000).

[122] K. Ono, M. Shuzo and M. Oshima, *Phys. Rev. B* **64** 085328 (2001).

[122] H. Tatsuoka, K. Isaji, H. Kuwabara, Y. Nakanishi, T. Nakamura, and H. Fujiyasu, *Appl. Surf. Sci.* **113**, 48 (1997).

[124] H. Tatsuoka, K. Isaji, K. Sugiura, H. Kuwabara, P. D. Brown, Y. Xin, and C. J. Humphreys, *J. Appl. Phys.* **83**, 5504 (1998).

[125] Y. Ashizawa, S. Saito, and M. Takahashi, *J. Appl. Phys.* **91**, 8096 (2002).

Chapter 2

Experimental facilities

2.1 Surface analytical techniques

The understanding of the physical and chemical properties of solid surface and interface is of great importance in many areas of science and technology, such as in material growth, chemical reactions and semiconductor processing [1]. A variety of surface sensitive techniques have been developed to investigate the surface with deep insights. For example, scanning tunneling microscopy (STM) enables scientist to visualize the solid surface in real space with atomic resolution. Low-energy electron diffraction (LEED) is an important technique for studying the atomic structure of crystalline surfaces in reciprocal space. Auger electron spectroscopy (AES) and X-ray photoelectron spectroscopy (XPS) are surface sensitive analysis tools used to study the chemical and electronic state of surface [2]. In this work, we have frequently used STM, AES and XPS, and a brief review of these techniques will be presented in the following.

2.1.1 Scanning tunneling microscopy

STM was introduced by G. Binnig and H. Rohrer at the IBM Zürich Research Laboratory in 1982 who were honored by the Noble Prize in 1986 [3]. It has become

widely used as an important instrument for real space analysis in surface science.

STM works based on quantum mechanical tunneling between a sharp tip and a conducting surface [4]. The basic idea is to bring a fine metallic tip (usually an etched tungsten wire) in close proximity (a few Å) to a conductive sample without actual physical contact, as shown in Figure 2.1. By applying a bias voltage (tens of *m*V to several V) between the tip and the sample,

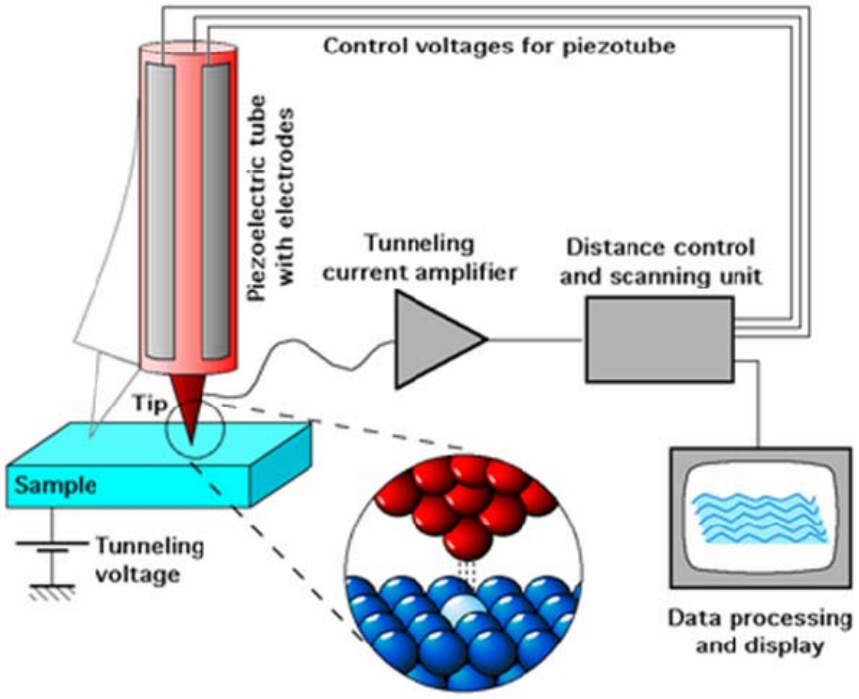

Figure 2.1 Schematic drawing of STM

a small tunneling current (0.01 nA-50 nA) can flow from the sample to the tip or reverse. As shown in Figure 2.2, if the distance between the tip and sample is *d* and a bias voltage *V* is applied, the tunneling current I can be written as:

$$I = bV \exp(-kd) \qquad (2.1)$$

where b and k are constants. It can be seen that I exponentially depends on *d* which leads to high resolution of STM. By scanning the tip controlled by a piezoelectrical tube across the surface and detecting the current, a map of the surface can be generated with a resolution in the order of atomic distances. It has to be mentioned that the image cannot be simply interpreted as a topographic map as the tunneling current is influenced by the lateral and vertical variation of the density of electronic state at the surface. The lateral resolution is about 1 Å whereas a vertical resolution up to 0.01 Å can be achieved.

There are two modes for STM imaging: constant height mode and constant current mode, as illustrated in Figure 2.3. For the constant current mode which is more frequently used, the feedback system keeps the tunneling current at a preset value. If the current exceeds the preset value, the distance (*d*) between tip and sample will increase, resulting in a decrease in the tunneling current. If the current falls below this value, the feedback will reduce the distance (*d*). Thus the tip is scanned line by line above the surface following the topography of the sample. In this way the image of

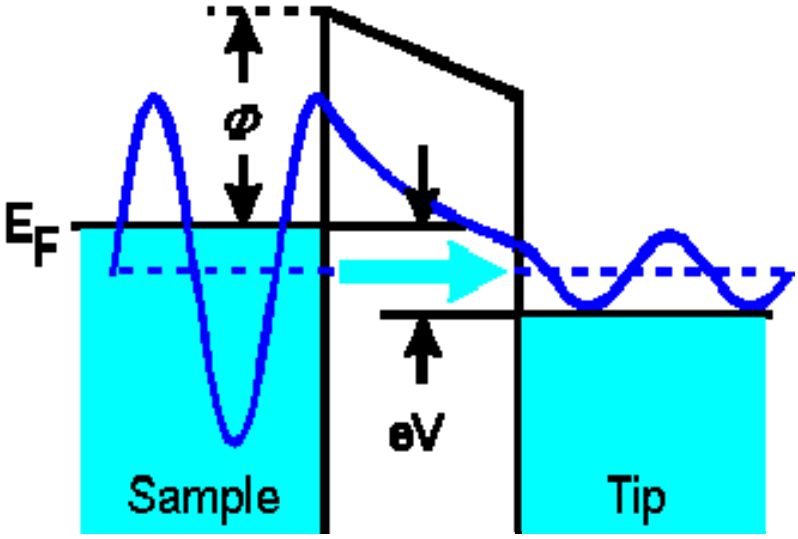

Figure 2.2 Energy level diagrams between tip and negative sample bias system

the sample surface can be obtained. In the constant height mode the vertical position of the tip is not changed, equivalent to a slow or disabled feedback. The current as a function of lateral position is used to construct a surface image. This mode is only appropriate for atomically flat surfaces as otherwise a tip crash would be inevitable. One of its advantages is that it can be used at high scanning frequencies (up to 10

kHz). In comparison, the scanning frequency in the constant current mode is usually less than 1 image per second.

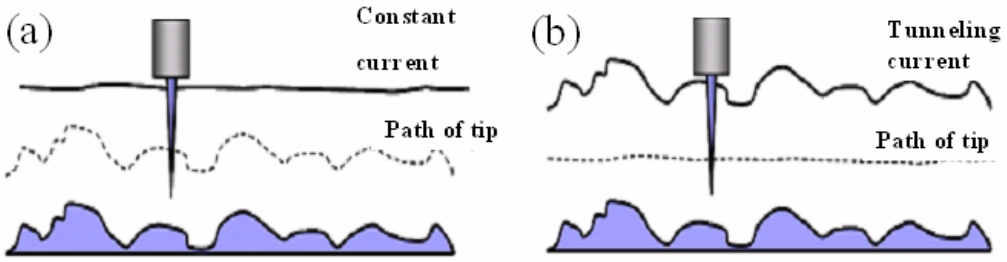

Figure 2.3 STM operational modes: (a) constant current mode and (b) constant height mode.

2.1.2 X-ray photoelectron spectroscopy

X-ray Photoelectron Spectroscopy (XPS), also known as ESCA (Electron Spectroscopy for Chemical Analysis), is an electron spectroscopic method that uses x-rays to eject electrons from inner-shell orbitals and then analyses their energy distribution [2]. It is a powerful surface analytical tool for determining the surface chemical and electronic states of solid samples. In our experiments, the XPS was mainly used to measure the chemical shifts in the binding energy of elements (e.g.

Mn, Sb, Si), in order to determine the reaction process and conditions between different elements.

A conventional XPS setup involves an X-ray source, typically Mg-Kα (1253.6 eV) or Al-Kα (1486.3 eV), and an electron energy analyzer (which can disperse the emitted electrons according to their kinetic energy, and thereby measure the flux of emitted electrons of a particular energy), with the experiment carried out in an ultra high vacuum (UHV) chamber as shown in Figure 2.4.

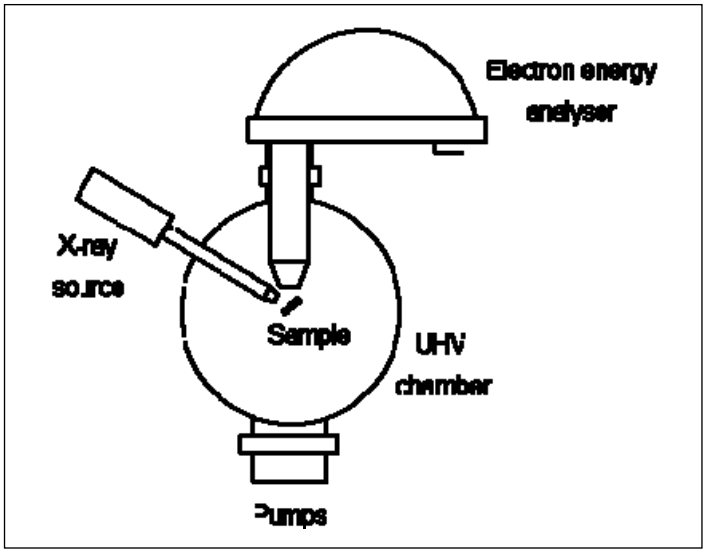

Figure 2.4 Schematic diagram of typical XPS setup.

The basic working principle of XPS is by photo-ionization of the core level electron of an atom using X-ray photons (Energy $h\nu$) generated from the X-ray source and then the kinetic energy (*KE*) of the emitted electrons is measured with the electron energy analyzer, in which the binding energy (*BE*) can be determined.

$$BE = h\nu - KE - \varphi \qquad (2.\ 2)$$

where φ refers to work function of the spectrometer analyzer. The binding energy of the electron is dependant on the chemical states of the element. Hence, by measuring the binding energy, it is possible to determine the chemical state of the sample, based on the relative shift in binding energy compared to that of the pure element or a known sample. For example, the binding energy of $2p_{3/2}$ of elemental Mn is located at 639 eV. However, in our experiment, when MnSb compounds were formed, such Mn $2p_{3/2}$ peaks shifted 2.6 eV toward higher binding energy with respect to the elemental peaks [5].

2.1.3 Auger Electron Spectroscopy (AES)

Auger Electron Spectroscopy (AES) was developed in the late 1960's , deriving its name from the effect first observed by Pierre Auger, a French Physicist, in the mid-1920's. It is a surface specific technique utilizing the emission of low energy electrons in the Auger process and is one of the most commonly employed surface analytical techniques for providing quantitative elemental analysis and some chemical state information of the surface.

The Auger process is a multi-electron event which involves transition between core and valence electron states. As shown in Figure 2.5, Auger spectroscopy can be considered as involving three basic steps :

(1) Atomic ionization (by removal of a core electron)

(2) Electron emission (the Auger process)

(3) Analysis of the emitted Auger electrons

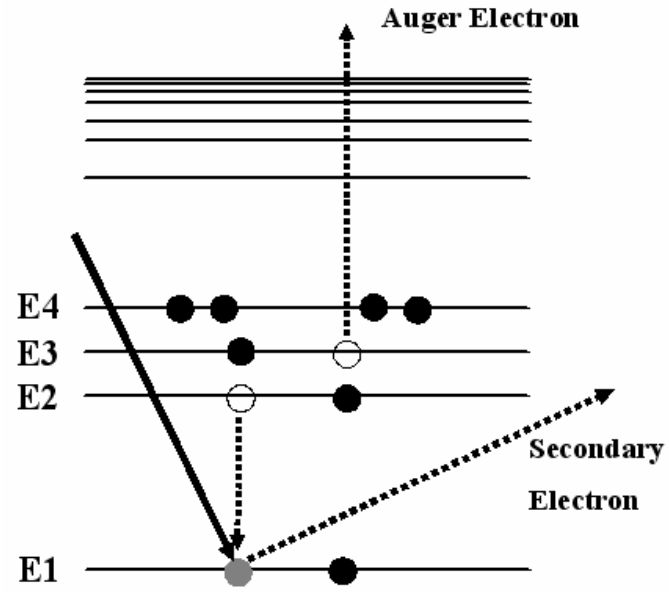

2.5 Schematic drawing for the process of emission of Auger electrons.

A sample is irradiated with a fine focused low energy (typically 5 - 10keV) electron beam in an ultra high vacuum chamber. Such electron beam have sufficient

energy to excite an electron from core level (E1), creating a hole or vacancy in the electron orbital. The ionized atom that remains after the removal of the core hole electron is in a highly excited state and the vacancy is subsequently filled by an electron with higher energy coming from the outer shell E2. The energy liberated in this process is simultaneously transferred to another outer shell (E3) electron. A fraction of this energy is required to overcome the binding energy of the electron in E3 level, and the remainder is retained by this emitted Auger electron as kinetic energy (E_{KE}). The Auger electron will be collected with an analyzer, where the E_{KE} and the intensity of Auger electron can be accurately measured. The E_{KE} of the Auger electron from the binding energies of the various levels involved can be accurately expressed as:

$$\mathbf{E_{KE} = (E1 - E2) - E3} \qquad (2.3)$$

Therefore, the kinetic energy of an Auger electron is characteristic of the core levels and valence band energies of the element from which it originated. The Auger electrons can be utilized to do a quantitatively analysis with the consideration of atomic sensitivity factors. The component of certain element A in a sample with homogenous composition can be determined using:

$$n = \frac{H_A / S_A}{\sum_i H_i / S_i} \qquad (2.4)$$

Where H_i and S_i represents the Auger peak intensity and the sensitivity factor for certain element, respectively. During our experiment, we commonly use AES to calibrate the flux rate of the sources and the relative ratio of elements (e.g. Mn and Sb). AES is a surface sensitive technique due to the strong inelastic scattering of electrons with energy ranging from 50-2500 eV. Consequently, it is an important technique for surface analysis.

2.2 Structural characterization

2.2.1 X-ray diffraction

X-ray diffraction (XRD) is a very important experimental technique that has long been used to address the issues related to the crystal structure of solid, including lattice constant and geometry, identification of unknown materials and orientation of single crystals [6]. In the XRD measurement, a monochromatic X-ray beam of wavelength λ (typically ranging from 0.7 to 2 Å) is incident on a crystal sample, as shown in Figure 2.6 The X-ray will be diffracted by the parallel periodic atomic planes with a spacing of *d*, according to the Bragg's Law:

$$2d\sin\theta = n\,\lambda \qquad (2.5)$$

The intensity of the diffracted X-ray is measured as a function of the diffraction angle 2θ and the sample's orientation. This diffraction pattern is used to identify the sample's crystalline phases and to measure its structural properties. As shown in Figure 2.7, the diffraction peak positions are accurately measured with XRD, which can be used to calculate the lattice constants of the crystals according to the Bragg Law.

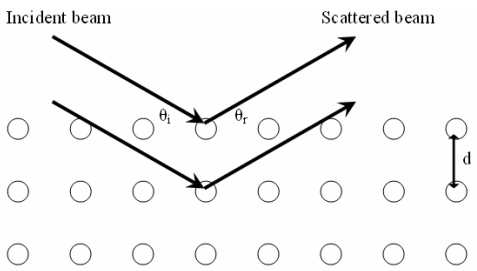

Figure 2.6 Schematics of XRD

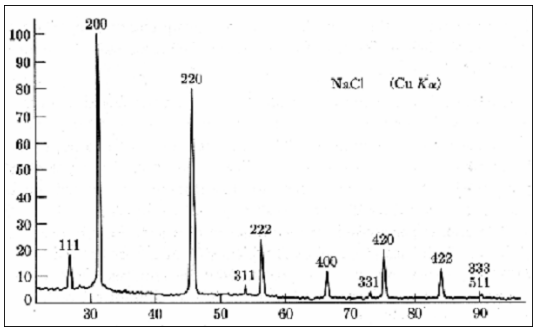

Figure 2.7 XRD pattern of NaCl powder

2.2.2 Transmission electron microscopy

In TEM, electrons are accelerate to 100 KeV or higher (up to 1 MeV), projected onto a very thin specimen (thickness less than 100 nm) by means of condenser lens

system. The electrons will transmit through the sample and an image is formed [7]. A schematic diagram of TEM is shown in Figure 2.8. The greatest advantages of TEM

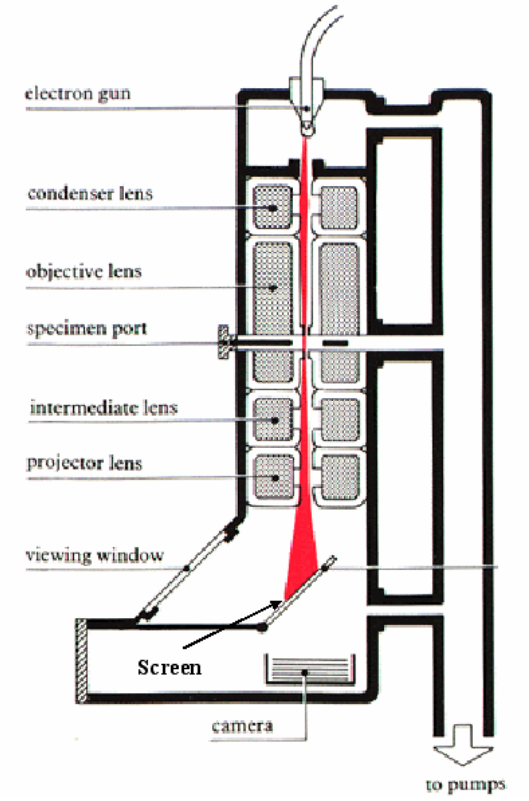

Figure 2.8 Schematic drawing of TEM

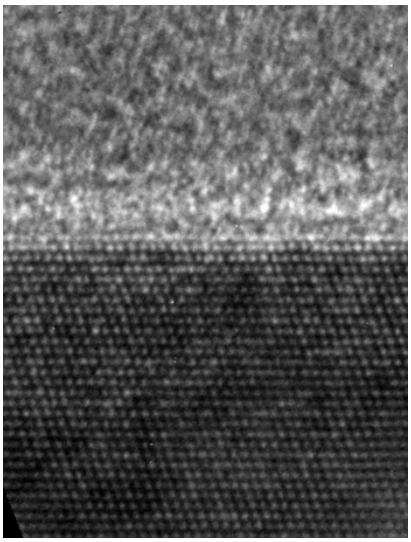

Figure 2.9 A high-resolution TEM image of Si(111) sample

are the high magnification and its ability to provide both image and diffraction information from a single sample. The high magnification or resolution of TEM is a result of the small effective electron wavelengths λ, which is given by the de Broglie relationship:

$$\lambda = \frac{h}{\sqrt{2mqV}} \qquad (2.6)$$

where m and q are the electron mass and charge, h is Planck's constant, and V is the potential difference through which electrons are accelerated. For example, electrons of 100 keV energy have wavelengths of 0.037Å. As a result, the short wavelengths of the electron in TEM make it achieve higher resolution. Typically, high voltage TEM instruments (e.g. 400 kV) have resolution better than 2 Å, which is enough for obtaining the atomic image of the sample. As shown in Figure 2.9, from an atomic TEM image of Si sample, the lattice structure and constant can be clearly identified. TEM is the most powerful tool to reveal the cross-sectional atomic structure of the interface.

Selected-area diffraction (SAD) also offers a unique capability to determine the crystal structure of individual nanostructures, such as nanocrystals and nanowires. In SAD, the condenser lens is defocused to produce parallel illumination at the specimen and a selected-area aperture is used to limit the diffraction volume. SAD patterns are often used to determine the Bravais lattice and lattice parameters of materials by the same procedure used in XRD.

One of the disadvantages of TEM is the difficulty in sample preparation which is critical to obtain high resolution images. Samples have to be mechanically sliced and polished, followed by ion milling to 100 nm thick for sufficient transmission. This process usually takes quite a long time and efforts to accomplish. Optimal instrumental setting such as defocus, sample alignment and illumination are also important to get high resolution images.

2.3 Magnetic characterization

Vibrating sample magnetometer (VSM) and superconducting quantum interference devices (SQUID) are widely used for the study of the magnetic properties of materials [6]. VSM is an equipment for the magnetic characterization of thin magnetic films and microstructures. After calibration, it is an absolute measure of the sample magnetization as a function of applied magnetic field and temperature with sensitivity of 5×10^{-6} emu. The basic working principle of VSM is schematically shown in Figure 2.10. Using a loud speaker, a magnetized sample is vibrated sinusoidally in a homogeneous magnetic field. Since the sample moves, the magnetic flux through the pick-up coils is altered and a voltage is induced. After calibration this voltage is directly proportional to the magnetic moment of the sample. Different magnetization under different magnetic field can be obtained. From the hysteresis loop, the saturation magnetization and coercivity of the samples can be readily acquired.

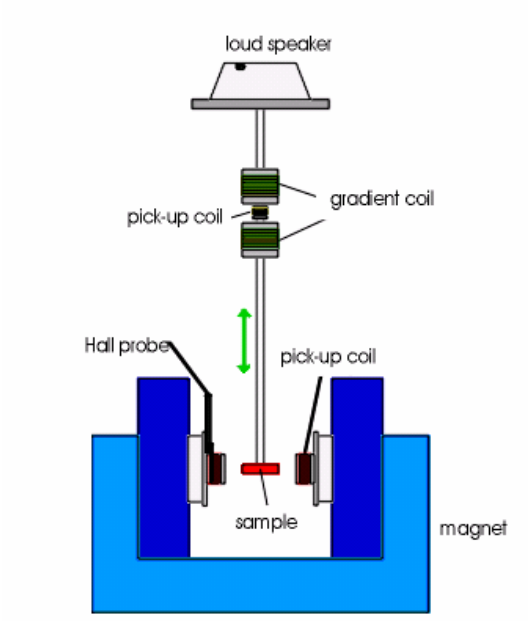

Figure 2.10 Schematic diagram of VSM system

However, the sensitivity of VSM is limited. It is usually not sensitive enough to probe the magnetic properties of nanostructures. SQUID are used to measure extremely small magnetic fields. They are one of the most sensitive magnetometers known. The magnetic measurement is typically done over a temperature range from that of liquid helium (~4K) to a couple of hundred degrees above room temperature, making it the most powerful tool to study the magentic properties of nanostructures.

2.4 Multi-probe UHV-STM setup

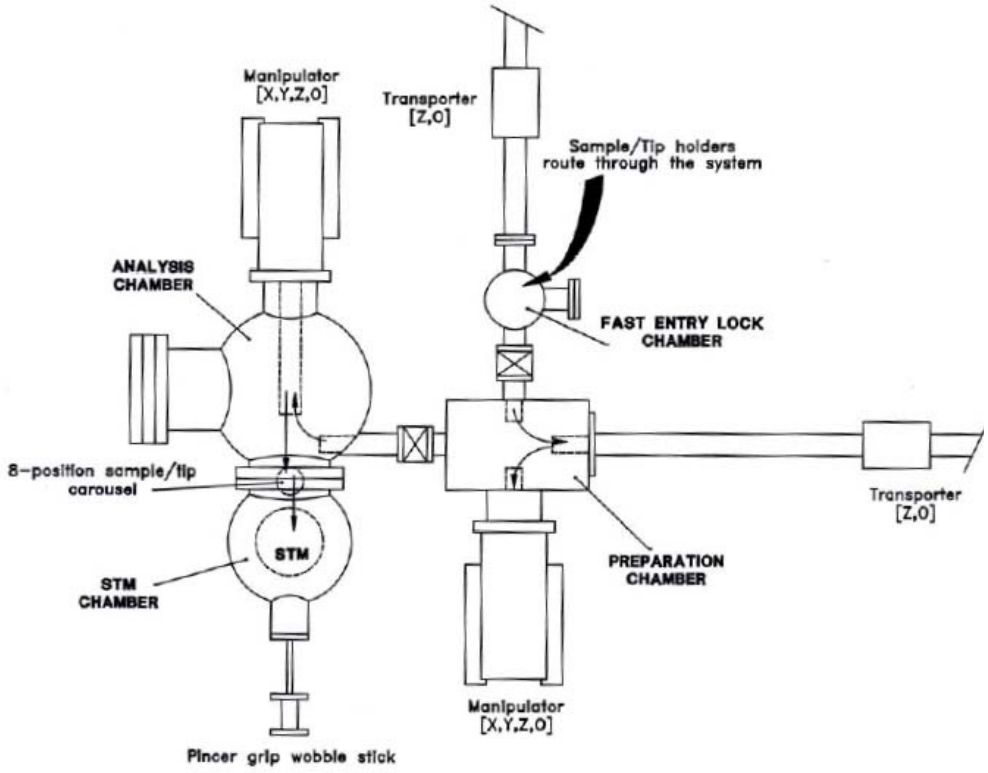

Figure 2.11 Schematic diagram of the UHV-STM system.

The preparation of MnSb compounds was carried out in an Omicron multi-probe UHV-STM system with a base pressure of 1×10^{-10} mbar. The vacuum is maintained by combination of turbomolecular pump and ion pumps. The top view of the system is shown in Figure 2.11. The analysis chamber is equipped with a STM (room temperature), four-grid optics for LEED and AES measurements to analyze the

surface order and the chemical composition. In addition, the system is equipped with manganese (Mn) and antimony (Sb) evaporators for materials growth. There is a fast entry load lock chamber for the introduction of samples and tips into the chamber without breaking the vacuum. Tungsten wires are used in the manipulators for the radiative sample heating below 700°C. For temperature above 700°C, electron beam bombardment heating is utilized. An infrared pyrometer is used to monitor the sample temperature. The photograph in Figure 2.12 shows different parts of the UHV-STM system.

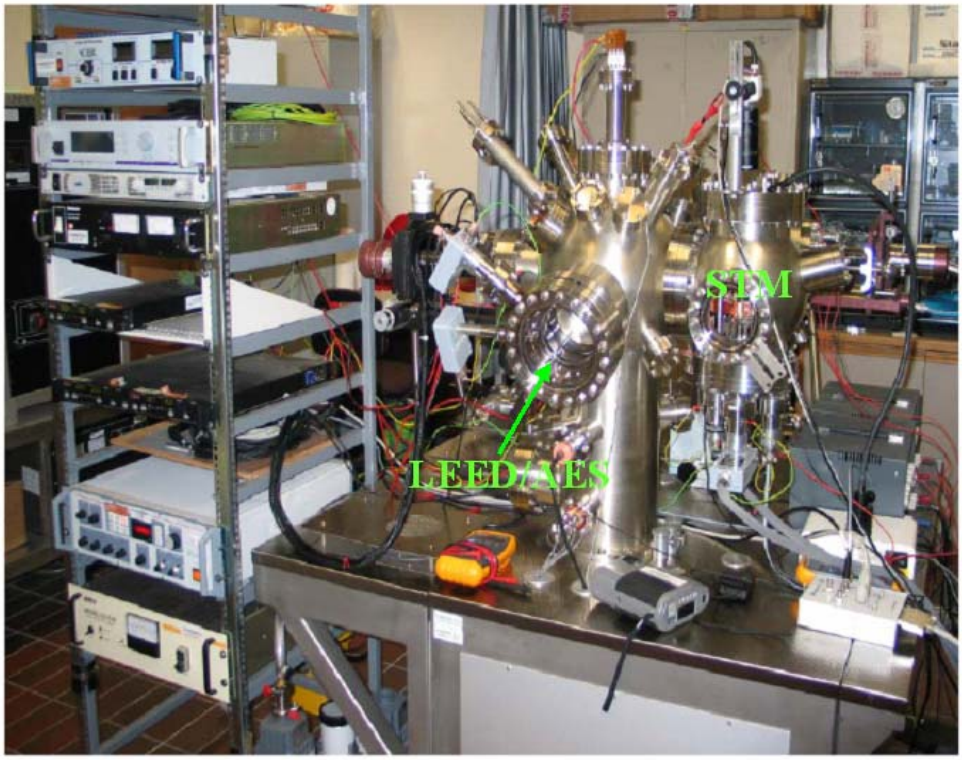

Figure 2.12 Photograph of the UHV-STM system.

Reference:

[1] S. C. Li, J. F. Jia, R. F. Dou, Q. K. Xue, I. G. Batyrev, and S. B. Zhang, *Phys. Rev. Lett.* **93**, 116103 (2004).

[2] J. C. Vickerman, S*urface Analaysis-The principal techniques*, Wiley, Chichester (1997).

[3] G. Binnig, H. Rohrer, Ch. Gerber, and E. Weibel, *Phys. Rev. Lett*. **50**, 120 (1983).

[4] J. Chen, *Introduction to Scanning Tunneling Microscopy*, Oxford University Press, New York (1993).

[5] B. L. Low, C. K. Ong, J. Lin, A. C. H. Huan, H. Gong, and T. Y. F. Liew *J. Appl. Phys.* **85**, 7340 (1999).

[6] C. Kittel, *Introduction to Solid State Physics,* 7th Edition, Wiley, New York (1996).

[7] S. L. Flegler, J. W. Heckman, K.L. Klomparens, *Scanning and Transmission Electron Microscopy: an Introduction,* W. H. Freeman, New York (1993).

Chapter 3

Growth and characterization of MnSb nano-crystallites and thin films on graphite

3.1 Introduction

As described in Section 1.3, manganese based compounds, such as maganese pnictides，chalcogenides and their alloys, have received considerable attention due to their attractive magnetic and magneto-optical properties. Especially, the ferromagnetic thin films, such as CuAu-type MnGa and NiAs-type MnAs [1-3], have been successfully fabricated on the leading semiconductor substrates such as Si, GaAs and InP by molecular beam epitaxy, offering attractive possibilities of fabricating new hybrid devices combining magnetic metal layers with semiconductor substrates [4-6]. α-phase manganese antimonide (α-MnSb) is one of the most promising ferromagnetic compounds with a Cure temperature of 317^{o}C [7]. It has strong magnetocrystalline anisotropy with the easy magnetization direction in the (0001) plane. Furthermore, MnSb is highly spin polarized, especially the zincblende-phase MnSb which is nearly half-metallic. A large magnetic Kerr rotation was reported from the near infrared to the visible wavelength range. The above-mentioned properties make MnSb a very promising

material in spintronic and magneto-optical applications. Recently, MnSb films and nanoparticles have been epitaxially grown on semiconductors such as GaAs and Si [8-11]. Intensive studies have been focused on the magnetic and interfacial properties. However, surface morphologies and atomic structures of these MnSb samples have not been examined carefully, although these factors are of crucial importance for better understanding of the growth and interface formation processes, as well as the magnetic properties. In addition, the growth of MnSb nanoparticles on GaAs and Si is strongly influenced by the substrates, and other compounds such as MnSi [10], often form in the growth process. A chemically inert material should provide a substrate to grow nearly free-standing nanoparticles and films with an abrupt interface, which should facilitate the exploration of surface morphologies and atomic structures. Such knowledge provides useful information to guide the epitaxy of MnSb compounds on semiconductor substrates.

Highly-oriented pyrolytic graphite (HOPG) is a prototypical inert substrate, and the study of the growth on HOPG sheds light on general behaviors of material growth on weak-bonding substrates [12]. Atoms or molecules deposited on an inert substrate normally form nanoparticles such as clusters or crystallites. Furthermore, these nanoparticles often line up along step edges of the substrate, forming quasi-one-dimensional (quasi-1D) chains or wires [13-15]. Such

magnetic nanoparticles [2,8,16-24] and quasi-1D magnetic structures [25-27] often exhibit novel magnetic properties induced by the finite-size and reduced dimensionality effects. Recently, MnSb and MnAs nanoparticles showing interesting magnetic properties have been successfully self-assembled on sulfur-passivated GaAs surfaces [18, 19]. Because the S-passivated GaAs had a relatively low surface energy, Volmer-Weber (3D islanding) growth model was observed. HOPG surface is non-reactive with a surface energy of only ~ 0.2 J/m^2, allowing aggregation of deposited atoms and nucleation of nanoparticles at the step edges.

In this chapter, we will discuss the growth of MnSb nano-crystallites and thin films on HOPG. The surface morphologies of these MnSb structures will be investigated using *in situ* scanning tunneling microscopy (STM). MnSb nano-crystallite chains with a typical width of 50 nm can be formed along the HOPG step edges. A continuous MnSb film is formed after Mn and Sb co-deposition on a HOPG pre-covered with an Sb wetting layer. The MnSb thin film surface exhibits mostly hexagonal-shaped MnSb(0001) plateaus with edges of a few atomic layers in height. Atomic-resolution STM images reveal 2×2 and ($2\sqrt{3}\times 2\sqrt{3}$)R30° reconstructions on the MnSb(0001) surface, and a 2×1 superstructure on MnSb($10\bar{1}1$). The chemical and magnetic properties were investigated with *ex situ* X-ray photoelectron spectroscopy (XPS) and vibrating sample magnetometry (VSM) measurements, respectively.

3.2 Experimental procedure

The growth of MnSb was performed in an Omicron multi-probe ultrahigh vacuum scanning tunneling microscope system (base pressure ~ 5×10^{-11} mbar) equipped with Ta-boat Mn and Sb evaporators. STM and Aüger electron spectroscopy (AES) were used for *in situ* growth monitoring. The typical growth rate is 8 Å/min. HOPG substrates (MaTecK, grade ZYB, mosaic spread 0.8°) cleaved in air and degassed at 400°C in UHV were used as substrates. Flat terraces of > 200 nm in width separated by steps were commonly observed on the HOPG substrates, as shown in Figure 3.1(a). For MnSb nano-crystallite growth, Sb and Mn were simultaneously evaporated onto clean HOPG at a substrate temperature of 150°C with a Sb/Mn ratio of 2 as calibrated with AES and STM. For MnSb thin film growth, Sb (~10 nm) and Mn (~10 nm) layers were successively deposited on the substrate at 100°C and annealed at 200°C for 5 min, followed by Sb and Mn co-evaporation onto the sample at 200°C with a Sb/Mn flux ratio of 2. After growth, STM images were taken at room temperature (RT) with electrochemically etched tungsten tips. The feature distortion in the images shown in this chapter due to thermal and mechanical drift as well as non-ideal tip shape has not been corrected. For further sample analyses, *ex-situ* XPS was recorded in a VG ESCALAB spectrometer using Mg *Kα* radiation (1253.6 eV). The magnetic hysteresis loop of a 50-nm MnSb film was measured with a VSM.

3.3 Results and discussion

3.3.1 Growth of Sb and Mn individually on HOPG

Recently we have studies the self-assembly of Sb nanostructures on HOPG. Three-dimensional (3D) spherical islands, 2D thin films and 1D nanorods of Sb can be formed by controlling the deposition flux and substrate temperature [14]. In particular, most of the nucleation and growth of spherical 3D islands occur at RT using a low flux. With a moderate flux, all three types of Sb structures grow initially, but further deposition leads to mostly the growth of 2D and 1D crystalline structures at RT as shown in Figure 3.1 (b). However, by increasing the substrate temperature and deposition flux, we are able to fabricate crystalline 2D Sb structures while suppressing 3D island formation. A typical STM image of Sb deposited on HOPG at 100°C is displayed in Figure 3.1(c), in which only 2D and 1D Sb structures are observed. Such samples were found suitable for later MnSb thin film growth. Atomic steps with average height of 3.85 ± 0.35 Å can be clearly resolved on 2D islands. A further zoom-in scan on the flat terrace reveals a hexagonal ordered atomic structure of Sb, with a periodicity of 4.22 ± 0.16 Å. Within experimental uncertainty, our measured values agree with the bulk α-Sb (111) values of step height (3.76 Å) and lateral period (4.31 Å) [28].

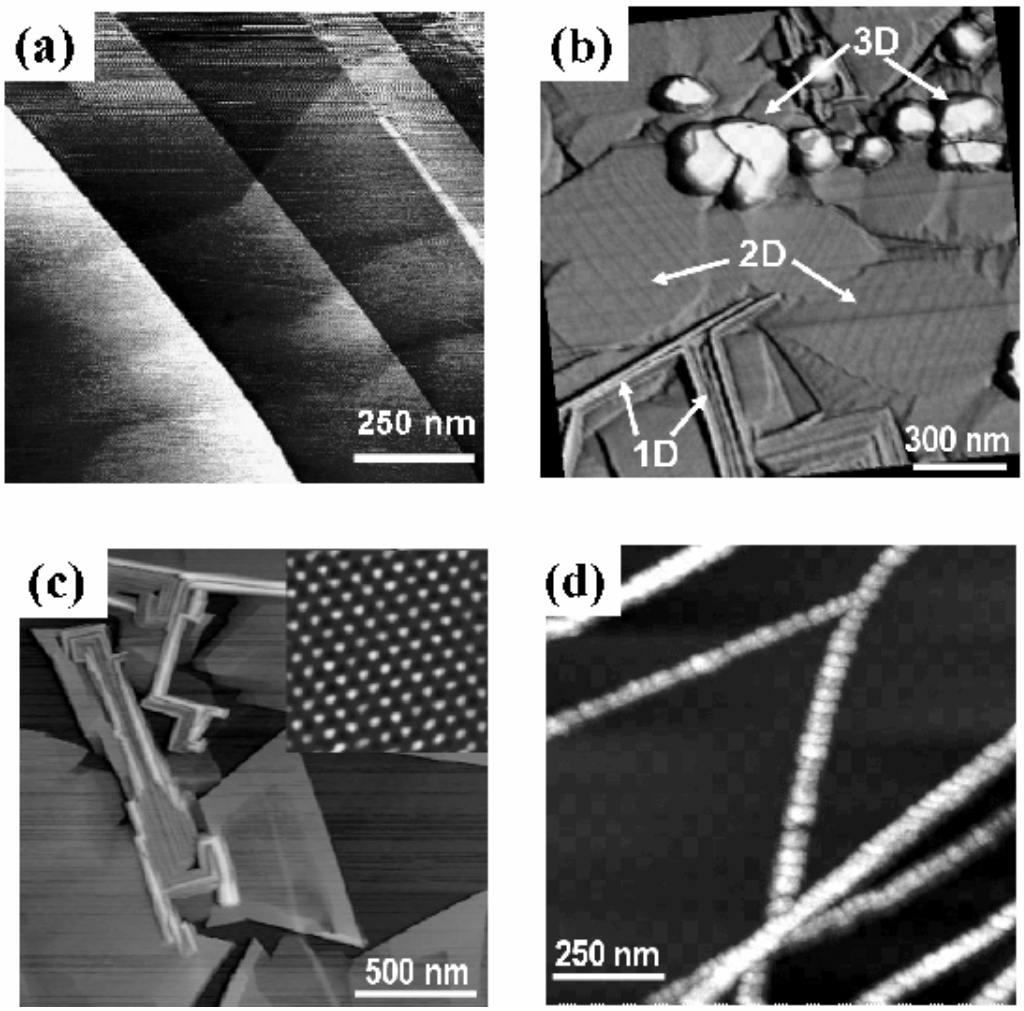

Figure 3.1 STM images of (a)Clean HOPG surface; (b) 10-nm Sb deposited on HOPG at room temperature, forming 1D nanorods, 2D wetting layer (covers most area), and 3D islands; (c) 5.4-nm Sb deposited at substrate temperature of 375 K, forming mostly 2D layers and some 1D nanorods; the inset (4 nm × 4 nm) shows zoom-in image on a 2D island; (d) Mn deposited at RT forming quasi-1D chains of linked 3D islands along HOPG steps.

For comparison, we also investigated the growth and morphology of Mn on HOPG. Figure 3.1(d) presents a STM image taken after Mn deposition on HOPG at RT. It is apparent that Mn forms quasi-1D chains of linked 3D islands along HOPG steps. No Mn clusters are observed on defect-free terraces. This indicates high mobility of Mn on HOPG even at RT and a weak interaction between Mn and HOPG. Only step edges can act as effective trapping sites for Mn adatoms and clusters, similar to the behaviors of other metals on HOPG such as Ag and Au [29, 30]. Unlike Sb, no wetting layer of Mn is observed on HOPG at or above RT.

3.3.2 Growth of MnSb nanocrystallites

Magnetic nanoparticles, nanowires and nanoparticle chains have been attractive topics due to the expectation of unique magnetic properties induced by the finite-size and reduced dimensionality effects at nano-scale [2,7,16-27]. The low surface energy of HOPG makes it a suitable substrate to grow MnSb nanoparticles. In addition, the step-edges on HOPG provide arrays of linear defect for trapping atoms and nanoparticles, enabling self-assembly of nanowires or chains of nanoparticles along them [12-15].

Figure 3.2(a) presents the morphology of MnSb nanoparticles on HOPG obtained with a Sb/Mn ratio of 2 at a substrate temperature of 150°C. MnSb

nanoparticles line up to form chains along HOPG step edges. The average width of the chains is about 50 nm and the average height is 25 nm, as illustrated by the profile plot in Figure 3.2(b). A zoom-in STM image in Figure 3.3(c) reveals the existence of flat facets on those MnSb nanoparticles, indicating that the MnSb nanoparticles are already crystalline, although we are not able to determine which facets they are. All MnSb nanocrystals locate exclusively at the step edges and none can be found in the defect free area, similar to the scenario of Mn as well as Ag and Au on HOPG [29-30]. This also indicates that the binding power on graphite terraces is too weak to hold the clusters even they may nucleate on the terraces. Mn atoms and Sb_4 have high mobility on HOPG defect-free terraces. Consequently, these atoms and probably small clusters nucleated on terraces can quickly arrive and finally settle at the step edges due to a stronger binding power at these sites. Later arriving atoms or small clusters will coalesce and react with the existing nucleus, leading to the growth of MnSb nanocrystals. The formation of the nanocrystal chains indicates that individual MnSb nanocrystals remain mobile along HOPG step edges, so that they can encounter and get linked with each other. When the step edges are fully occupied by MnSb nanocrystallites, MnSb nanoparticles can be observed on the terraces after more deposition.

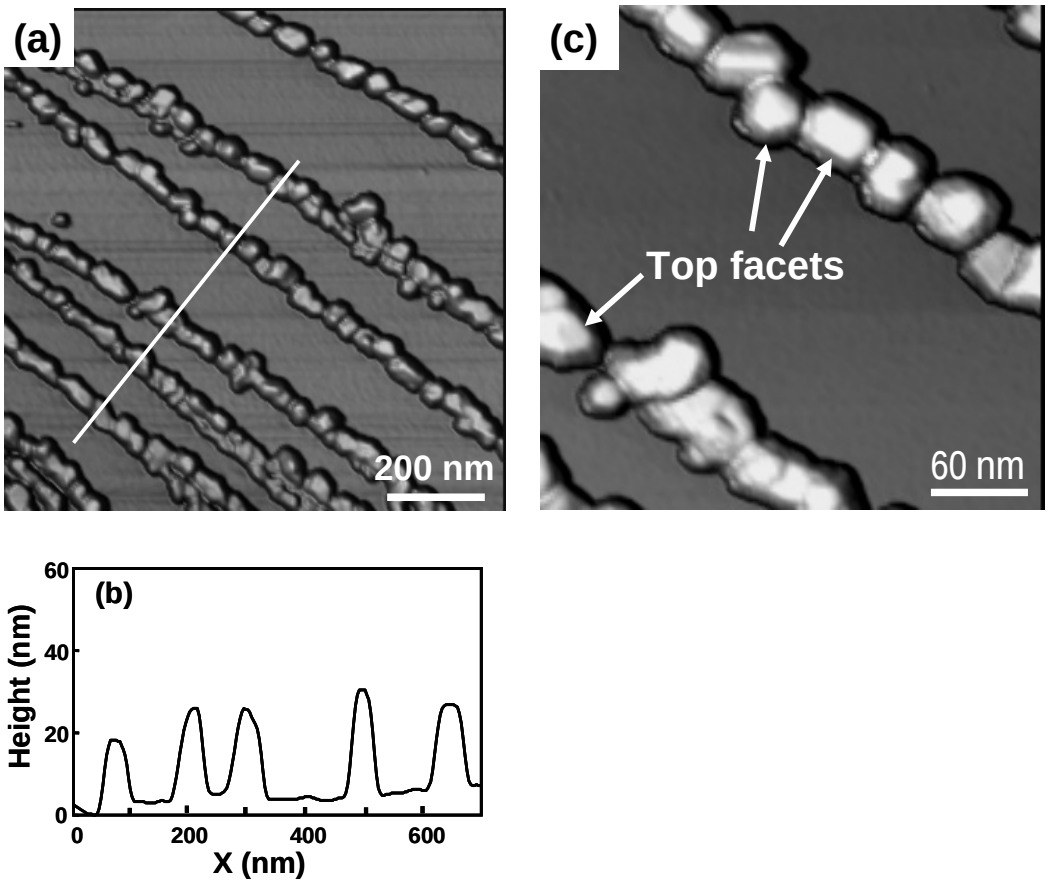

Figure 3.2 (a) STM image of MnSb nano-crystallite chains positioned along HOPG step edges, with average height 20 nm and width 50nm; (b) height profile along the line; (c) a zoom-in image showing facets on the MnSb nano-crystallites.

3.3.3 MnSb thin film morphology and surface reconstructions

To grow MnSb thin film, we first deposited 10 nm Sb and 10 nm Mn consecutively at 100°C, followed by Sb and Mn co-deposition onto the sample at 200°C with a Sb/Mn flux ratio of 2. According to the results shown in Figure

3.1(c) and our previous work [11], most of the HOPG surface should be covered with Sb(111) thin film after 10-nm Sb deposition. The 10-nm Mn deposited next is able to react with the Sb film to form compound mainly with α-MnSb(0001) aligned with the substrate surface. The (0001)-oriented MnSb film grows dominantly with subsequent Sb and Mn co-deposition at 200°C. Figure 3.3(a) presents a STM image of a MnSb film sample. The average film thickness is approximately 50 nm. Figure 3.3(a) shows many hexagonal-shaped atomically flat islands. The edges of these hexagonal-shaped terraces are mostly 5.8 ± 0.2 Å or 11.6 ± 0.2 Å in height, corresponding to the monolayer or bilayer steps on MnSb(0001) [31], respectively. Similar surface morphology has also been observed for MnAs epilayers on As-terminated GaAs($\bar{1}\bar{1}\bar{1}$), which showed well defined triangular and hexagonal blocks with MnAs(0001) plane. These features in the STM image indicate that our film is truly α-MnSb with the c-axis of MnSb lattice dominantly perpendicular to the film surface. Rüdiger *et al.* [32] reported that, with successive deposition of Bi and Mn, MnBi thin films grew on fused quartz with c-axis perpendicular to the surface, reflecting the similarities among these Mn pnictides [33].

Our STM images with atomic resolution on top of these hexagonal terraces provide further lattice parameter information of the film. The period of the hexagonal lattice observed on the surface is 8.3±0.2 Å, as marked by the

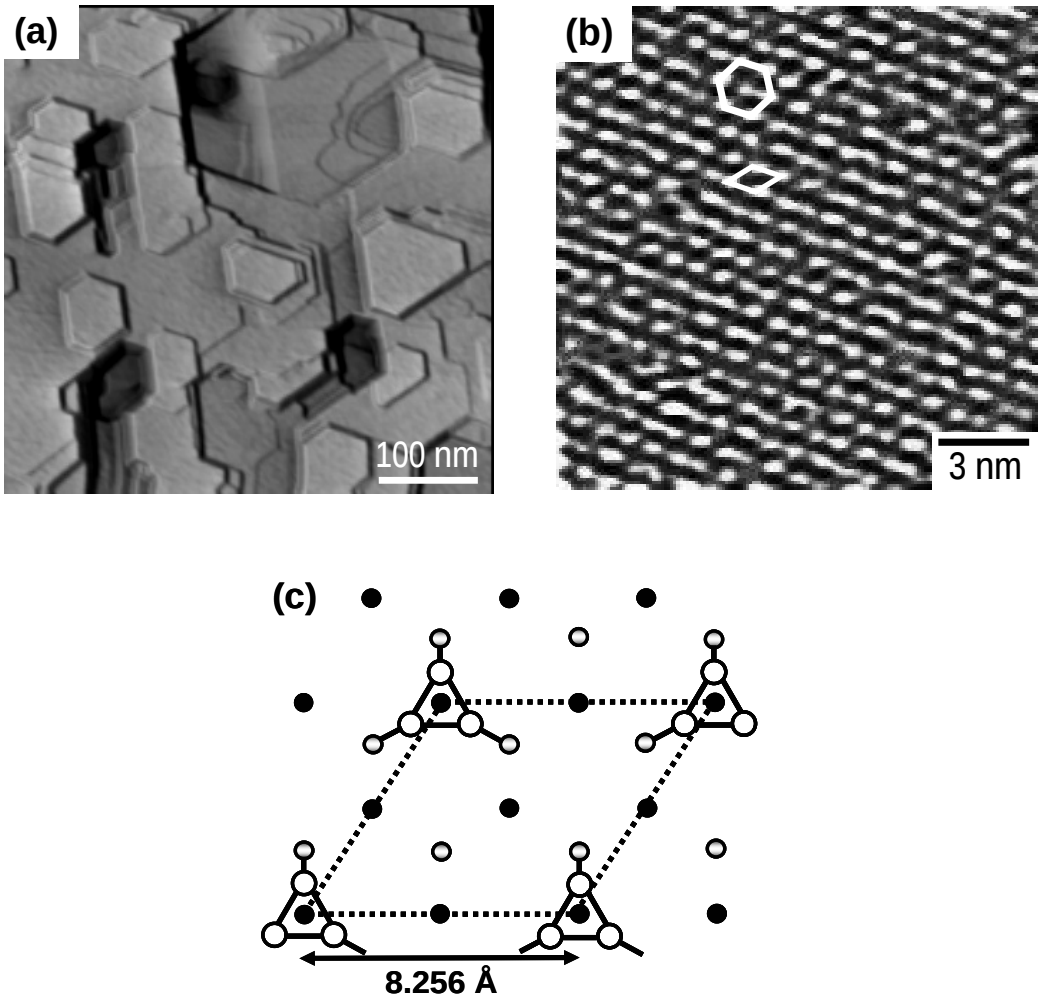

Figure 3.3 (a) Surface morphology of MnSb film with thickness of ~ 50 nm grown on HOPG and (b) zoom-in image taken on a hexagonal terrace, a 2×2 cell is outlined with a diamond; (c)atomic model of MnSb(0001)-2×2 reconstruction with Sb trimers on top, with large open circles denoting Sb trimers, small shaded circles the first layer Sb atoms and small filled circles the Mn atoms below. The STM imaging parameters: sample bias V_S = -1.1 V and tunneling current I_T = 0.3 nA in (b)

diamond and hexagon in Figure 3.3(b). Considering the lattice constant a = 4.128 Å with a 3-fold symmetry on MnSb(0001), we assign the observed surface structure as MnSb(0001)-2×2 reconstruction. Previous *in-situ* STM studies on MnAs epitaxilly grown on GaAs($\bar{1}\bar{1}\bar{1}$) also reported a 2×2 reconstruction of MnAs(0001) [2, 34]. Due to the similarity between MnSb and MnAs, it is reasonable that they show similar surface superstructure.

It is well known that in the growth of III-V semiconductor compounds, the III/V ratio of deposition flux plays an important role in determining the surface structure formed. This is also true for the growth of MnSb and MnAs. In our case, since the samples were grown under Sb-rich condition and annealed under Sb flux, the surfaces were likely Sb-terminated. This assumption is confirmed by the XPS result presented in the following section which shows excess elemental Sb peaks. Analogous to the GaAs($\bar{1}\bar{1}\bar{1}$)-2×2 As-trimer model of Biegelsen *et al*.[35], an As-trimer model was proposed by Kästner *et al.* for MnAs(0001)-2×2 reconstruction [27]. A similar Sb-trimer model, in which the Sb adatoms bond strongly with each other to form the trimers and these trimers bond to the first-layer Sb atoms, may be suitable for the MnSb(0001)-2×2 reconstruction observed here. The atomic model of such a MnSb(0001)-2×2 reconstruction with Sb trimers is sketched in Figure 3.3(c).

Besides the 2×2 reconstruction, we observed other surface superstructures

on the MnSb(0001) facets.. For example, we also observed the 3×1 row structure reported by Ouerghi *et al*.[2] for MnAs grown on GaAs($\bar{1}\bar{1}\bar{1}$). Additionally, some new surface structures have been found on our MnSb/HOPG samples. Figure 3.4(a) is an STM image taken from another area of the MnSb film shown in Figure 3.3(a). The measured period along the arrow direction is 14.5±0.3 Å, which fits the cell size of ($2\sqrt{3}\times 2\sqrt{3}$)R30° superstructure within the experimental uncertainty. With a sample bias of -0.7 V and a tunneling current of 0.35 nA, the ($2\sqrt{3}\times 2\sqrt{3}$)R30° superstructure appears as periodically positioned units along the [$10\bar{1}0$] directions with each unit consisting of three bright spots. Due to drift and irregular tip shape, the features are distorted in the STM image. Figure 3.4(b) is a schematic drawing showing the orientational alignment of the ($2\sqrt{3}\times 2\sqrt{3}$)R30° superstructure with respect to MnSb substrate lattice. Since the detailed atomic configuration of the ($2\sqrt{3}\times 2\sqrt{3}$)R30° reconstruction is unknown, the lateral registry of the bright spots with respect to the MnSb substrate (represented by the small circles) is not necessarily that in the drawing.

In addition to the dominant (0001) surface, ($10\bar{1}1$) facets have been observed occasionally on the MnSb film grown on HOPG. The ($10\bar{1}1$) facet has been observed on samples of MnAs or MnSb grown on common semiconductor substrates such as Si(111), Si(001) and GaAs(001) [10, 36-38]. Figure 3.5(a) is a

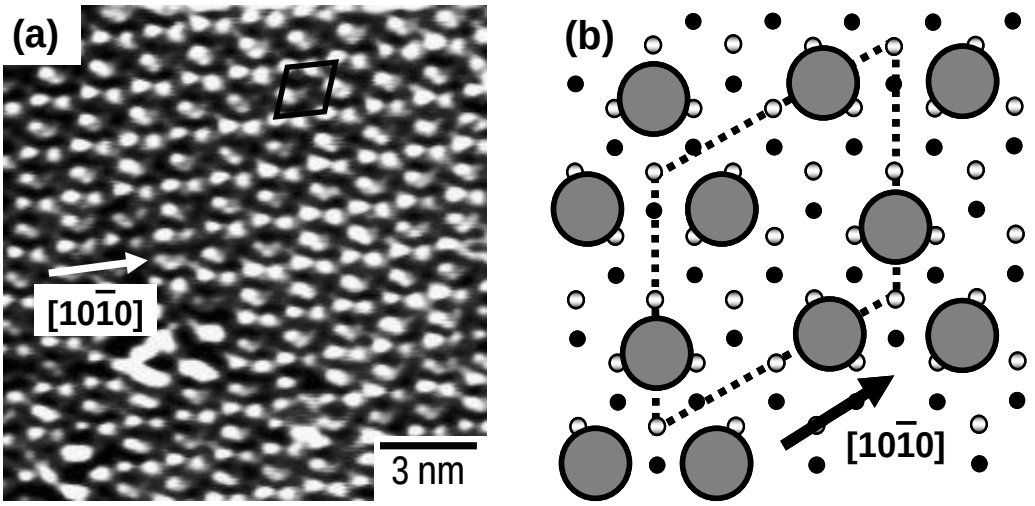

Figure 3.4 (a) A STM imag (taken with V_S = -0.7 V and I_T = 0.35 nA) of another MnSb(0001) area showing the ($2\sqrt{3}\times 2\sqrt{3}$), with the diamond representing the unit cell and the arrow pointing along the $[10\bar{1}0]$ direction. (b) Schematics of ($2\sqrt{3}\times 2\sqrt{3}$)R30° superstructure on MnSb(0001) with the super-cell outlined by the dot-line diamond and large circles representing the bright spots in STM image. The small open and filled circles represent the substrate lattice.

STM image of a $(10\bar{1}1)$-faceted area on the MnSb film. The atomic steps on the surface have a measured height of 3.15±0.15 Å, in agreement with the expected value (3.042 Å). The atomic structure on the terraces appears as rows, with more details revealed in the small-area image of Figure 3.5(b). The measured row

spacing is 13.4±0.4 Å, which is about twice of the lattice period in the $[\bar{1}012]$ direction (i.e., 6.804Å). The period along the rows is 4.20±0.10 Å. Therefore, the $(10\bar{1}1)$ surface is (2×1)-reconstructed with the rows running along the $[1\bar{2}10]$ direction.

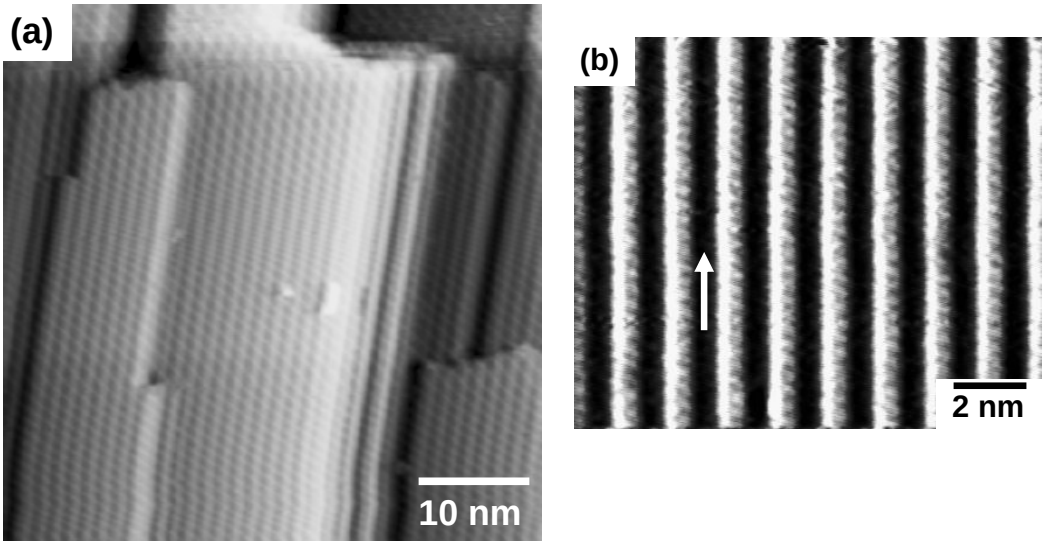

Figure 3.5 (a) STM image of a $(10\bar{1}1)$-faceted area on the MnSb film. (b) a zoom-in scan of 13 nm × 11 nm of MnSb$(10\bar{1}1)$ terrace taken with V_S = -1.1 V and I_T = 0.7 nA. The arrow points to the $[1\bar{2}10]$ direction.

3.3.4 Electronic and chemical state analyses with XPS

The core level photoemission spectra of transition metals, with satellite or multiplet structures caused by Coulomb or exchange interaction between core

holes and valence band electrons, can provide us with electronic structural information [39]. In order to investigate the electronic and chemical states of our MnSb thin film and nanocrystallite samples, we analyzed X-ray photoemission spectra as displayed in Figure 3.6. The wide survey scan in Figure 3.6(a) for the 50-nm film reveals the presence of Sb, Mn, C and O. Narrow-scan Mn and Sb core level spectra were taken to extract more electronic state information. Compared with elemental Mn, the Mn 2*p* spectrum of MnSb compound [Figure 3.6(b)] shows: (1) the same spin-orbital splitting energy (~11.8 eV) between Mn $2p_{3/2}$ and Mn $2p_{1/2}$ at 641.5 eV and 653.3 eV, respectively; (2) a shift of 2.5 eV towards higher binding energies with respect to the elemental Mn peaks, indicating the formation of MnSb compound [8]. Ono *et al.* reported that the Mn 2*p* spectra of MnAs nanoscale dots were quite different from the Mn 2*p* of MnAs films, due to the localization of Mn 3*d* electrons in the dots [19]. In our studies, we have not observed significant difference between the Mn 2*p* of the thin film and nanocrystallite samples. One possible reason is that our MnSb crystallites are much larger than the MnAs dots reported by Ono *et al.*, which are 10 nm in diameter and 2-5 nm in height. Comparing with those dots, our MnSb crystallites are close to the bulk. Furthermore, the MnAs dots in their report were in zincblende lattice, whereas our MnSb crystallites are most likely in NiAs-type lattice. In addition, the Mn $2p_{3/2}$ component is accompanied by a satellite

structure at 647.5 eV marked as Shake-up in Figure 3.6(b). A similar satellite structure is also observed in the Mn 3*p* (48 eV) at the 49.4 eV [see Figure 3.6(c)]. These satellite structures can be attributed to plasma satellite [39].

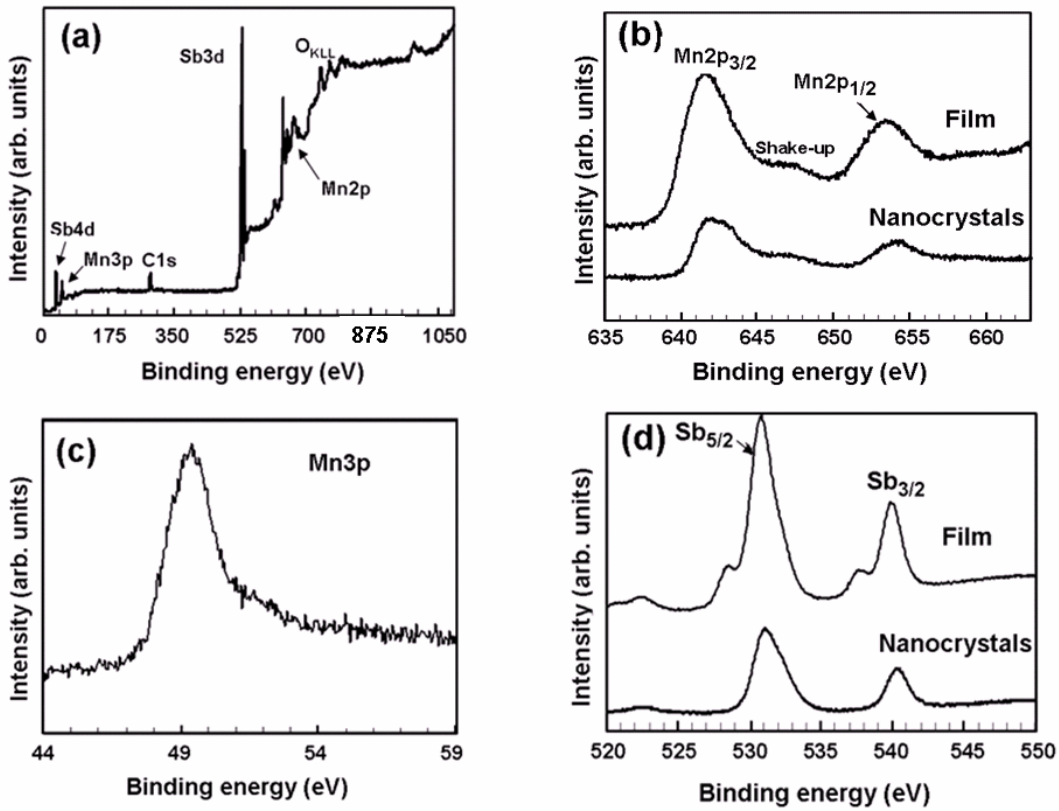

Figure 3.6 Core-level XPS spectra of MnSb (a) wide scan; (b) Mn 2*p* doublet of MnSb thin films (top) and MnSb nanocryatllites (bottom); (c) Mn 3*p* spectrum of MnSb thin films; (d) Sb 3*d* spectra of MnSb thim films(top) and nanocrystallites (bottom).

As for Sb [Figure 3.6(c)], the 3*d* doublets with a separation of 9.3 eV show a shift of ~ 2 eV toward higher binding energy for both MnSb thin film and crystallite chain samples, further supporting the formation of MnSb compound. Since O 1*s* core level resides at the same binding energy range as Sb $3d_{5/2}$, the Sb $3d_{5/2}$ peak shows a broad structure. As a result, the ratio of the integrated peak area of $I_{5/2}$:$I_{3/2}$ is a little larger than 3/2. Because of the excess Sb environment during deposition and annealing, the elemental Sb peaks are observed at 528 eV and 537 eV for MnSb thin film sample. A higher substrate temperature during deposition or post-deposition annealing can be used to get rid of the excess Sb.

3.3.5 Magnetic measurement

VSM measurement with applied magnetic field parallel to the HOPG surface shows that the MnSb film is ferromagnetic at RT (Figure 3.7). From the magnetic hysteresis loop, the saturation magnetization (M_s), remanent magnetization (M_r) and coercivity (H_c) are determined after carefully subtracting the diamagnetic background from sample holder and HOPG substrate. It is found that our MnSb film shows a saturation total magnetic moment of 0.6×10^{-3} emu and can be easily magnetized (H_c = 120 Oe). Considering a sample thickness of ~ 50 nm and an area of 25 mm^2, the saturation magnetization M_s is about 480 emu/cm^3. These values are comparable to those reported by Tatsuoka *et al.*[40]

for MnSb on Si(111) (they found the easy magnetization axis in MnSb(0001) plane). It demonstrates the high structural quality of MnSb thin film in terms of crystalline phase and *c-axis* alignment, and it further supports our conclusion based on STM surface structural studies that α-MnSb film has been synthesized with MnSb(0001) parallel to HOPG basal plane. The VSM was not sensitive enough to measure the magnetic behavior of the crystallite chain sample shown in Figure 3.2(a).

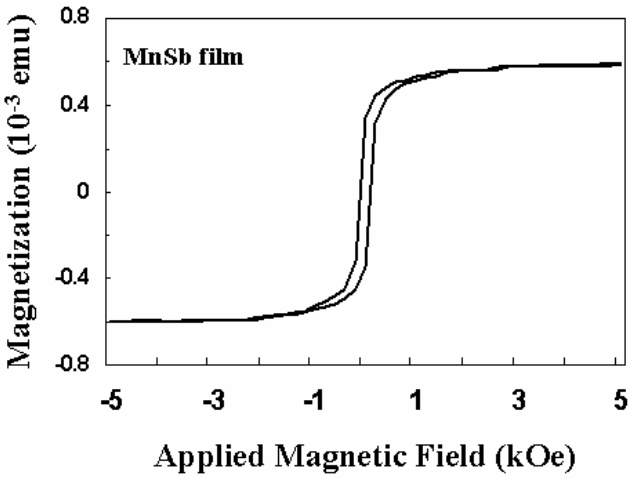

Figure 3.7 Hysteresis loop of 50-nm thick MnSb film on HOPG measured by VSM at RT with an applied magnetic field in the film plane.

3.4 Summary

In summary, we have synthesized chains of nanocrystallites and thin films

of ferromagnetic MnSb on HOPG by co-evaporating Mn and Sb in UHV. *In situ* STM studies revealed that the MnSb thin film surface is dominantly MnSb(0001) exhibiting a 2×2 reconstruction. Other surface superstructures such as MnSb(0001)-($2\sqrt{3}\times 2\sqrt{3}$)R30° and MnSb($10\bar{1}1$)-2×1 have also been observed. Our XPS data showed that the Mn 2*p* peaks shift 2.5 eV with respect to elemental Mn, and Sb 3*d* peaks shift 2 eV, indicating the formation of MnSb compound. VSM measurement at RT revealed that the MnSb film was ferromagnetic with a high saturation magnetization and a small coercivity.

Reference:

[1] K.M. Krishnan, *Appl. Phys. Lett.* **61**, 2365 (1992).

[2] A. Ouerghi, M. Marangolo, M. Eddrief, S. Guyard, V.H. Etgens, and Y. Garreau, *Phys. Rev. B* **68**, 115309 (2003).

[3] A.M. Nazmul, A.G. Banshchikov, H. Shimizu, and M. Tanaka, *J. Cryst. Growth* **227**, 874 (2001).

[4] G.A. Prinz, *Science* **250**, 1092 (1990).

[5] S. Sun, C.B. Murray, D. Weller, L. Folks, and A. Moser, *Science* **287**, 1989 (2000).

[6] M. Tanaka, *Semicond. Sci. Technol.* **17**, 327 (2002).

[7] H. Akinaga, M. Mizuguchi, K. Ono, and M. Oshima, *Appl. Phys. Lett.* **76**, 2600 (2000).

[8] B.L. Low, C.K. Ong, G. C. Han, H. Gong, T.Y.F. Liew H. Tatsuoka, H. Kuwabara, and Z. Yang, *J. Appl. Phys.* **84**, 973 (1998).

[9] B.L. Low, C.K. Ong, J. Lin, A.C.H. Huan, H. Gong, and T.Y.F. Liew *J. Appl. Phys*. **85**, 7340 (1999).

[10] H. Tatsuoka, K. Isaji, K. Sugiura, H. Kuwabara, P.D. Brown, Y. Xin, and C.J. Humphreys, *J. Appl. Phys.* **83**, 5504 (1998).

[11] Y. Ashizawa, S. Saito, and M. Takahashi, *J. Appl. Phys.* **91**, 8096 (2002).

[12] C.R. Henry, *Surf. Sci. Rep.* **31**, 231 (1998).

[13] R.M. Penner, *J. Phys. Chem. B* **106**, 3339 (2002).

[14] X.-S. Wang, S.S. Kushvaha, Z. Yan, and W. Xiao, *Appl. Phys. Lett.* **88**, 233105 (2006).

[15] X.-S. Wang, W. Xiao, S.S. Kushvaha, Z. Yan, and M. Xu, in: E.V. Dirote (ed.), *New Development in Nanotechnology Research* (Nova Science, New York, 2006), Chap. 6.

[16] H. Akinaga, J. De Boeck, G. Borghs, S. Miyanishi, A. Asamitsu, W. Van Roy, Y. Tomioka, and L.H. Kuo, *Appl. Phys. Lett.* **72**, 3368 (1998).

[17] M. Moreno, A. Trampert, L. Däweritz, and K.H. Ploog, *Appl. Surf. Sci.* **234**, 16 (2004).

[18] M. Mizuguchi, H. Akinaga, K. Ono, and M. Oshima, *J. Appl. Phys*. **87**, 5639 (2000).

[19] K. Ono, J. Okabayashi, M. Mizuguchi, M. Oshima, A. Fujimori, and H. Akinaga, *J. Appl. Phys.* **91**, 8088 (2002).

[20] P. J. Wellmann, J.M. Garcia, J.-L. Feng, and P.M. Petroff, *Appl. Phys. Lett.* **73**, 3291 (1998).

[21] Sh.U. Yuldashev, Y. Shon, Y.H. Kwon, D.J. Fu, D.Y. Kim, H.J. Kim, T.W. Kang, and X. Fan, *J. Appl. Phys.* **90**, 3004 (2001).

[22] H. Akinaga, M. Mizuguchi, K. Ono, and M. Oshima, *Appl. Phys. Lett.* **76**, 2600 (2000).

[23] J. Okabayashi, M. Mizuguchi, K. Ono, M. Oshima, A. Fujimori, H. Kuramochi, and H. Akinaga, *Phys. Rev. B* **70**, 233305 (2004).

[24] C. Binns, S.H. Baker, C. Demangeat, and J.C. Parlebas, *Surf. Sci. Rep.* **34**, 105 (1999).

[25] C.L. Dennis, R.P. Borges, L.D. Buda, U. Ebels, J.F. Gregg, M. Hehn, E. Jouguelet, K. Ounadjela, I. Petej, I.L. Prejbeanu, and M.J. Thornton*, J. Phys.: Condens. Matter* **14**, R1175 (2002).

[26] J. Shen, J.P. Pierce, E.W. Plummer, and J. Kirschner, *J. Phys.: Condens. Matter* **15**, R1 (2003).

[27] M.J. Hÿtch, R.E. Dunin-Borkowski, M.R. Scheinfein, J. Moulin, C. Duhamel, F. Mazaleyrat, and Y. Champion, *Phys. Rev. Lett.* **91**, 257207 (2003).

[28] J. Donohue, *The Structures of the Elements* (Wiley, New York, 1974).

[29] G. M. Francis, L. Kuipers, J.R.A. Cleaver, and R.E. Palmer, *J. Appl. Phys.* **79**, 2942 (1996).

[30] B. Blum, R.C. Salvarezza, and A.J. Arvia, *J. Vac. Sci. Technol. B* **17**, 2431 (1999).

[31] V.H. Etgens, M. Eddrief, D. Demaille, Y.L. Zheng, and A. Ouerghi, *J. Cryst. Growth* **240**, 64 (2002).

[32] U. Rüdiger, P. Fumagalli, P. Dworak, A. Schirmeisen, and G. Güntherodt, *J. Appl. Phys.* **79**, 6203 (1996).

[33] H.-M. Hong, Y.-J. Knang, J. Kang, E.-C. Lee, Y.-H. Kim, and K.J. Chang, *Phys. Rev. B* **72**, 144408 (2005).

[34] M. Kästner, L. Däweritz, and K.H. Ploog, *Surf. Sci.* **511**, 323 (2002).

[35] D.K. Biegelsen, R.D. Bringans, J.E. Northrup, and L.-E. Swartz, *Phys. Rev. Lett.* **65**, 452 (1990).

[36] Y. Ashizawa, S. Saito, and M. Takahashi, *J. Appl. Phys.* **91**, 8096 (2002).

[37] K. Akeura, M. Tanaka, M. Ueki, and T. Nishinaga, *Appl. Phys. Lett.* **67**, 3349 (1995).

[38] H. Akinaga, S. Miyanishi, W. Van Roy, J. De Boeck, and G. Borghs, *Appl. Phys. Lett.* **73**, 3285 (1998).

[39] S. Hüfner, *Photoelectron Spectroscopy: Principles and Applications* (Springer, Berlin, 2003).

[40] H. Tatsuoka, K. Isaji, H. Kuwabara, Y. Nakanishi, T. Nakamura, and H. Fujiyasu, *Appl. Surf. Sci.* **113**, 48 (1997).

Chapter 4

Growth of MnSb on Si(111)

4. 1 Introduction

The realization of spintronic devices relies on the effective combination of magnetic materials with the common semiconductors (i.e. GaAs and Si), so that the so-called magnetic/semiconductor hybrid structure can be fabricated. Over the past few decades, ferromagnet/semiconductor hybrid structures have been attracting much interest as a new class of electronic materials, because of their potential in novel device applications based on the integration of spintronics and semiconductor electronics [1, 2]. Quite some research groups have been very active in the epitaxial growth of elemental magnetic thin films of Co and Fe on semiconductor substrate, since these materials are useful in the Schottky barrier spin-injection devices [3]. Intensive efforts have also been devoted to the epitaxy of Mn-based compounds such as MnAs, MnSb, MnAl and MnGa on semiconductor substrates [3-8], as mentioned in Chapter 1. For example, ferromagnetic MnAs thin films grown on GaAs substrate have been extensively studied, yielding high quality epitaxial films by molecular beam epitaxy (MBE) [4]. The high quality ferromagnetic films act as spin injection sources in semiconductor device structures. More advanced magnetic tunnel junctions (MTJ)

with MnAs/AlAs/MnAs trilayers have been fabricated on GaAs for tunneling magnetoresistance devices operating at room temperature, which is desirable for high performance magnetoresistive random access memory (MRAM) [9]. Recently, the epitaxial growth and characterization of MnSb on GaAs have been carried out by several groups [10-15]. Low *et al.* [7,15] studied the structural, morphological and magnetic properties of MnSb epitaxial layers grown on GaAs(001). Akinaga *et al.* [16] reported more than 1000% positive magnetoresistance effect in MnSb nanoparticles grown on S-passivated GaAs substrates. On the other hand, only a few works have been done for MnSb grown on Si substrate, although it will be highly desirable to combine ferromagnetic layers with Si so that Si-based spintronic devices become possible. Tatsuoka *et al*. [17] studied MnSb(0001) growth on Si(111) by hot wall epitaxy. The crystal structure and interface properties were investigated by transmission electron microscopy (TEM) and X-ray diffraction (XRD). However, surface morphology and chemical states of the films have not been examined carefully, although these factors are of crucial importance for better understanding of the growth process and magnetic properties.

In this chapter, we study the growth of MnSb on Si(111) substrate at different substrate temperature ranging from 200°C to 300°C. The effect of temperature on the surface morphologies and crystal structure were studies using

in situ STM and XRD. The interfacial properties at different temperatures were examined using TEM and X-ray photoelectron spectroscopy (XPS) techniques.

4.2 Experimental procedure

The growth of MnSb was performed in the Omicron multi-probe ultrahigh vacuum scanning tunneling microscope system (base pressure ~ 5×10^{-11} mbar). Atomically clean Si(111)-7×7 surface was prepared by degassing the Si(111) sample at 600°C for several hours followed by flashing at 1200°C for 1 minute. Then the sample was rapidly cooled to 900^{o}C, followed by slow cooling to room temperature. This procedure routinely yields a clean Si(111)- 7×7 as confirmed by LEED and STM. MnSb films were grown by simultaneously evaporating Sb and Mn onto Si(111)-7×7 surface with a Sb/Mn flux ratio of 2.5 and a typical deposition rate of 3 Å/min. The substrate temperatures (T_{sub}) were varied from 200°C to 300°C. STM was used to study the morphology and surface atomic structures of grown MnSb films. To analyze the chemical states of deposited films, *ex-situ* XPS was recorded in a VG ESCALAB spectrometer using Mg *Kα* radiation (1253.6 eV). The interface and crystal structures were characterized with cross-sectional TEM and the θ-2θ X-ray diffraction (XRD) scan using Cu *Kα* radiation (λ = 1.541 Å).

4.3 Results and discussion

4.3.1 Surface morphology and crystal structure

In Figure 4.1, we present our STM images and a XRD spectrum of MnSb grown on Si(111) at T_{sub} = 200°C. According to the morphology revealed with STM, MnSb takes three-dimensional (3D) islanding growth model on Si(111)-7×7. A similar islanding growth model has also been observed for MBE growth of MnAs on Si(111) by Nazmul *et al.* [18] From thermodynamic point of view, this growth model is due to the high surface energy of MnSb and a weak interface bonding. In early stage of growth，as shown in Figure 4.1(a), two types of clusters can be distinguished. The first type is small spherical MnSb clusters with an average diameter of 10 nm and an average height of 4 nm. When the size of the clusters is small, they tend to take a spherical shape to reduce the surface energy. The second type is larger clusters with diameters of 20 nm or more. Zoom-in STM images showed that these large clusters already exhibit flat facets on top.

In Figure 4.1(b), further growth and subsequent coalescence of MnSb are evident after 10 nm deposition. Here, we also observed two types of MnSb grains, as marked Type A and B in Figure 4.1(b). The Type A grains have relatively low profile with flat top facets. Their lateral sizes are in the range of 40–100 nm. Most of Type A grains are interconnected with one another. Inset of Figure 4.1(b) is a high resolution STM image on the top surface of a Type A grain. It reveals a

nearly rectangular order with a measured unit cell size of 7.2 Å × 11.6 Å. As described in detail later, this surface structure is probably the 1×2 reconstruction on α-MnSb(11$\bar{2}$0). The Type B MnSb grains have an average lateral size of 40 nm and 10 nm in height.

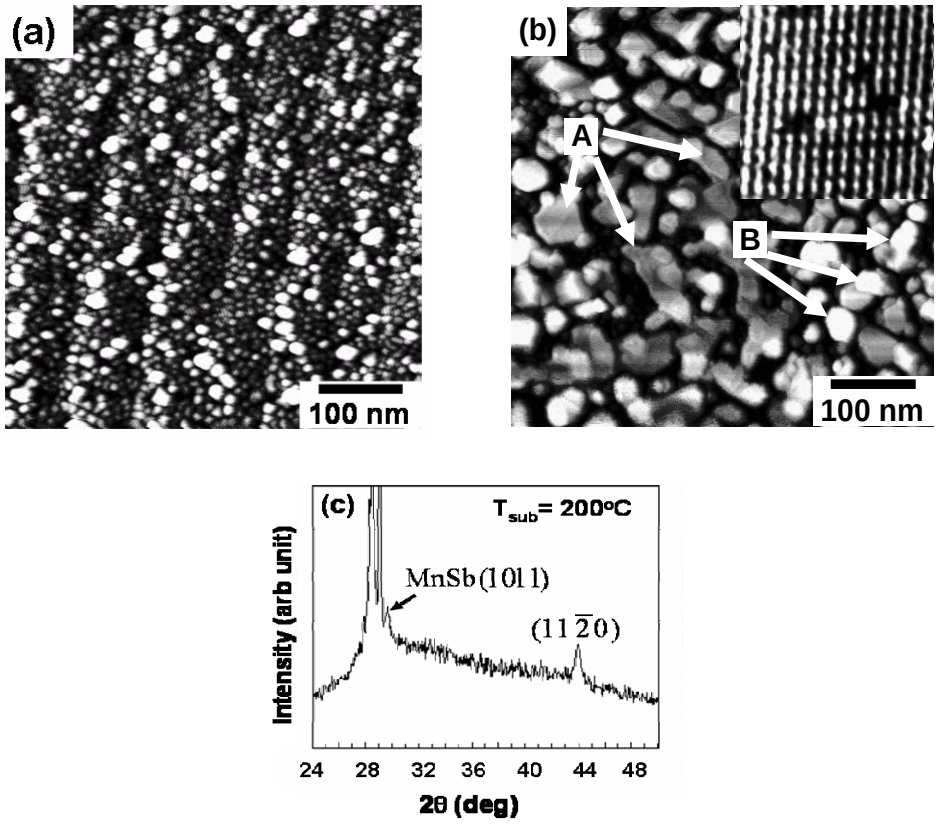

Figure 4.1 Evolution of MnSb morphology on Si (111) at 200°C with increasing deposition nominal thickness: (a) 2 nm, (b) 10 nm, (c) zoom-in scan on the top facet of a type A island; (d) θ-2θ XRD spectrum of sample shown in (b).

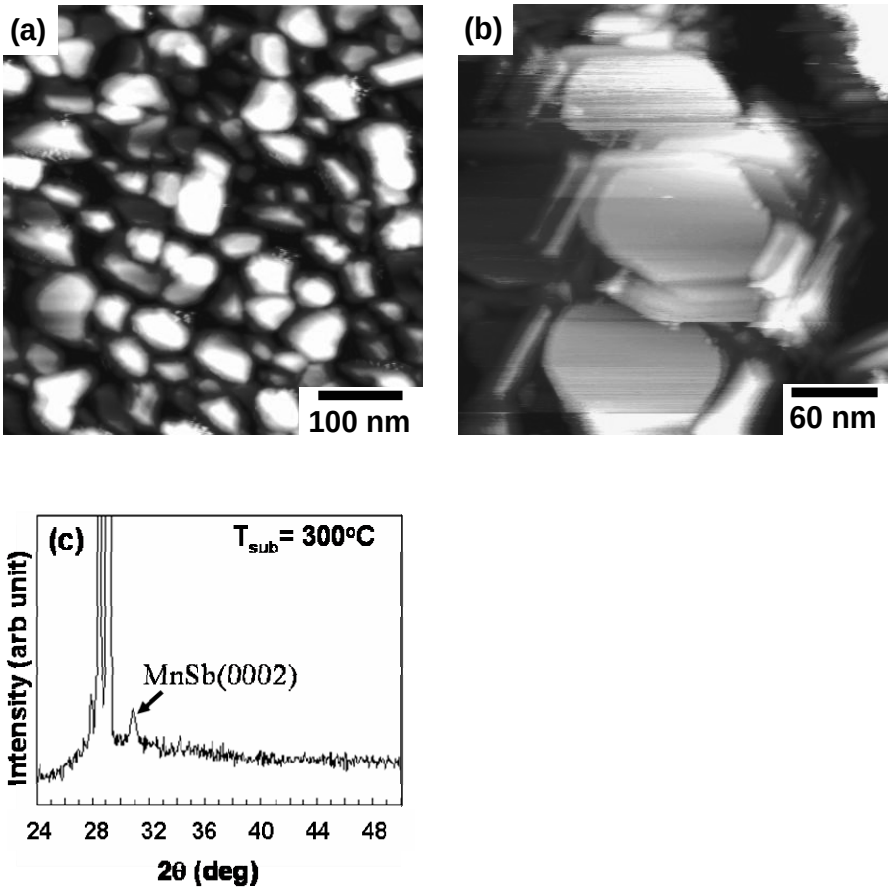

Figure 4.2 Evolution of MnSb morphology on Si(111) at 300°C with increasing deposition nominal thickness: (a) 2 nm, (b) 10 nm; (c) θ-2θ XRD spectrum of sample shown in (b).

Figure 4.1(c) shows a typical XRD spectrum of the MnSb sample grown at T_{sub} = 200°C with 10 nm deposition. There are three peaks in this spectrum. The peak at 28.4° comes from Si(111) substrate. The other two peaks at 29.5° and 43.9° are identified as the diffraction of $(10\bar{1}1)$ and $(11\bar{2}0)$ planes of MnSb. It

indicates that two types of MnSb crystallite orientations are preferred at T_{sub} = 200°C, namely MnSb(10$\bar{1}$1) ‖ Si(111) and MnSb(11$\bar{2}$0) ‖ Si(111). The same diffraction peaks were observed by Ashizawa *et al*. [19] when MnSb films were grown on Si(111) at T_{sub} = 200°C by sputter deposition. Now, let us examine Figure 4.1(b) again. Since the in-plane periodicity of MnSb(11$\bar{2}$0) without reconstruction is 7.15 Å × 5.78 Å, within experimental uncertainty the surface structure obtained is MnSb(11$\bar{2}$0) with 1 × 2 reconstruction. Hence, we conclude that the Type A islands are MnSb films with (11$\bar{2}$0) plane parallel to the substrate and the Type B are MnSb grains with (10$\bar{1}$1) parallel to Si(111).

When the substrate temperature is kept at 300°C, the surface morphology and crystallite orientation are different from that grown at 200°C. Figure 4.2 shows the STM images and a XRD spectrum of MnSb grown at T_{sub} = 300°C. It can be seen in Figure 4. 2(a) that large MnSb islands appear on the surface at the early stage. These islands, typically 50 nm in lateral size, have nearly hexagonal flat facets on top. With 10 nm deposition, large hexagonal islands of typical size 100 nm can be found as shown in Figure 4.2(b). Considering the 3-fold symmetry on MnSb(0001), we believe that these are (0001)-topped MnSb crystallites. In the last chapter, we presented the morphologies and atomic structure of MnSb thin film grown on graphite. STM images showed that MnSb(0001) on graphite exhibited essentially hexagonal-shaped plateaus, same as the morphology

observed here. Indeed, the peak at 2θ = 30.9° in the XRD spectrum of Figure 4.2(c) corresponds to MnSb(0002). It is confirmed that MnSb epitaxial layers with MnSb(0001) ‖ Si(111) are grown on Si(111) at T_{sub}= 300°C. XPS and TEM measurements presented later indicate that these MnSb islands are not all formed on Si(111) directly, but with a MnSi layer in between.

4.3.2 Chemical states and interfacial structure

It is generally difficult to grow Mn-based compounds with sharp interface on Si substrates, because Mn atoms can react with Si to form MnSi at the interface [6,13,17,20,21]. Tatsuoka *et al.* [17] reported a 10 nm MnSi interfacial layer formed when MnSb was grown on Si(111) at 300^{o}C. For the growth of MnAs on Si [6], it was considered that MnSi compounds at the interface degraded the quality of MnAs films. Hence, the growth conditions should be carefully controlled in order to optimize the interfacial layer and correspondingly to improve the quality of MnSb or MnAs films. Accordingly, we used XPS and cross-sectional TEM to characterize the interfaces between MnSb and Si(111) at different growth conditions. Figure 4.3(a) shows the Mn 2*p* XPS spectrum for MnSb grown on Si(111) at various temperatures. It can be seen that for T_{sub} in 200-300 °C range, the binding energies of Mn $2p_{3/2}$ and Mn $2p_{1/2}$ are located at 641.6 eV and 653.4 eV, respectively. These Mn 2*p* peaks shifted 2.6 eV toward

higher binding energies with respect to the elemental peaks, indicating the formation of MnSb compound [7]. When the substrate temperature is 200°C, only Mn 2*p* coming from MnSb can be detected by XPS, without the presence of MnSi. This is confirmed by the TEM image in Figure 4.3(b), which shows that MnSb islands have sharp interface on Si(111) with little interfacial reaction. This is probably due to that 200°C is not enough to activate the migration of Mn and Si for silicide formation [20, 21]. At T_{sub} = 250°C, however, a shoulder can be observed at 639.6 eV. This shoulder is ascribed to MnSi formed by solid phase reaction. TEM image [Figure 4.3(b)] also shows that the interface is not sharp. More MnSi formation can be seen in XPS when T_{sub} is 300°C.

4.3.3 Discussion

In early stage of MnSb growth on Si(111), there is competition between the formations of MnSb and $MnSi_x$. It has been reported that the selective growth of one particular intermetallic phase is governed by both kinetic and thermodynamic factors [22]. According to Zhang and Ivey [23], Mn is the main diffusing species during the solid phase epitaxy of MnSi on Si. A substrate temperature of 200°C is not high enough for Mn to overcome the barrier to diffuse into Si and react with it. Moreover, the sticking coefficient of Sb (mostly Sb_4 in our experiment) is large at low temperature. Mn atoms will react readily with Sb

to form MnSb compound, hence MnSb formation is favorable in this condition. This scenario is illustrated in Figure 4.4(a).

On the other hand, at $T_{sub} \geq 250°C$, Mn atoms are significantly activated to diffuse into and react with Si substrate. Furthermore, more Sb atoms (or Sb_4) will

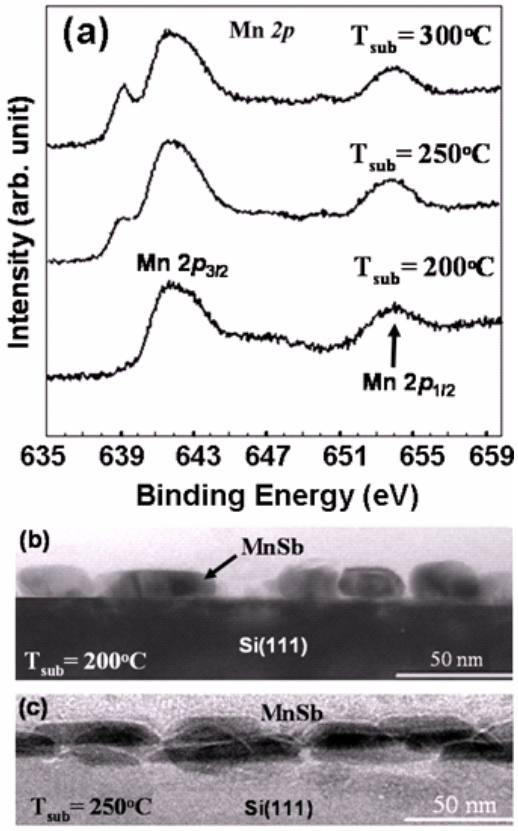

Figure 4.3 (a) Core-level XPS spectra of Mn *2p* of MnSb thin films deposited at 200°C (bottom), 250°C (middle) and 300°C (top). (b) TEM image of MnSb deposited at 200°C. (c) TEM image of MnSb deposited at 250°C.

desorb at higher temperature. Therefore, MnSi interfacial layer is formed at the beginning [Figure 4.4(b)]. When the thickness of MnSi layer has reached a certain value, it can retard the in-ward diffusion of Mn. Then, Mn atoms will react with Sb to form MnSb [Figure 4.4(c)]. MnSi takes cubic FeSi crystalline structure with a lattice constant of 4.556 Å. The high resolution TEM study by Tatsuoka *et al.* [17] reported that the thin MnSi layer was rotated 30^{o} with respect to Si with MnSi(111) ‖ Si(111) and MnSi[$1\,\bar{2}\,1$] ‖ Si[$0\,\bar{1}\,1$]. The lattice mismatch between MnSi and Si(111) was reduced to only 3%. Both MnSi(111) and MnSb(0001) possess a threefold symmetry, and furthermore they have Mn as the common element. As a consequence, MnSb(0001) epitaxial growth on MnSi(111) and subsequently on Si(111) is possible in this condition.

4.4 Conclusions

In summary, we have studied the growth process of MnSb on Si(111) at substrate temperatures ranging from 200°C to 300°C. Our results show that the formation of MnSb layers proceeds in 3D island growth model on Si(111). At T_{sub} = 200°C, MnSb crystallites with ($10\,\bar{1}\,1$) or ($11\,\bar{2}\,0$) planes parallel to Si(111) were observed. TEM and XPS measurements showed that the interface between MnSb and Si is sharp without interfacial reaction at 200°C. When grown at 300°C, initially Mn can react with Si substrate, forming a thin MnSi epitaxial layer. Later,

MnSb crystallites grow with (0001) plane on the MnSi layer.

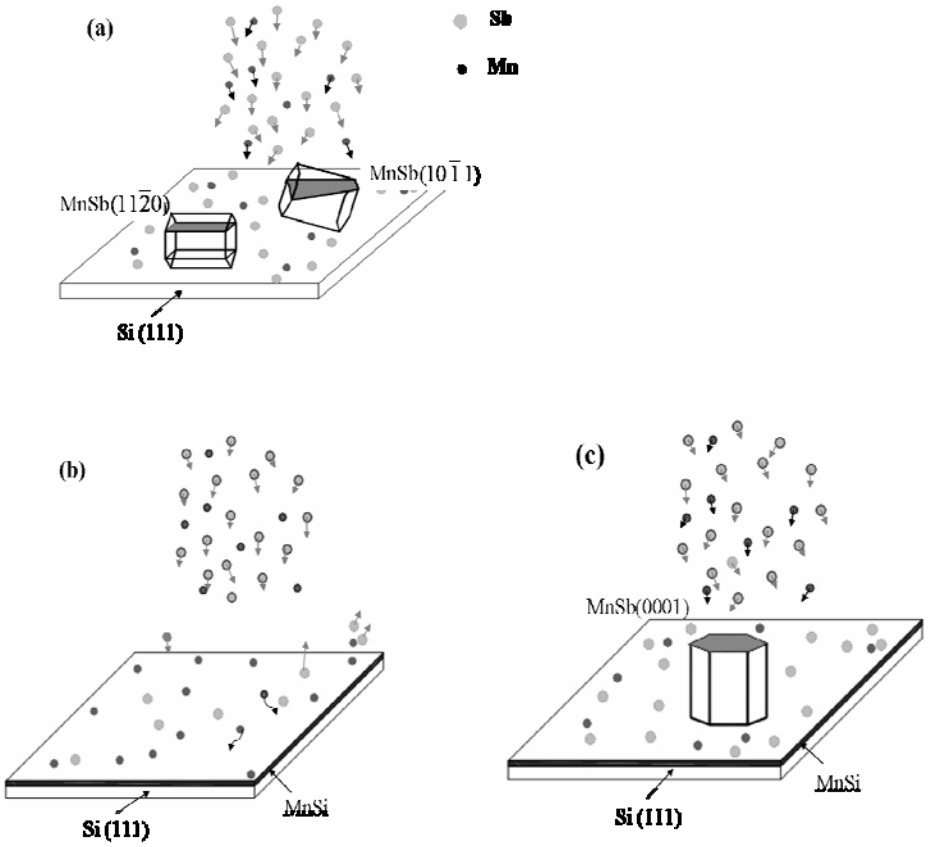

Figure 4.4 Schematic growth models of MnSb on Si(111) at different substrate temperature: (a) MnSb(10 $\bar{1}$ 1) and (11 $\bar{2}$ 0) planes are grown directly on Si(111) at 200°C; (b) at 300°C, Mn diffuses into the substrate to form MnSi; (c) MnSb(0001) grows epitaxially on MnSi.

References:

[1] G. Prinz, *Science* **250**, 1092 (1990).

[2] M. Tanaka, *Semicond. Sci. Technol.* **17**, 327 (2002).

[3] J. A. C. Bland and B. Heinrich, *Ultrathin magnetic structures, I and II* (Springer, Berlin, 1994).

[4] A. Ouerghi, M. Marangolo, M. Eddrief, S. Guyard, V.H. Etgens, and Y. Garreau, *Phys. Rev. B* **68**, 115309 (2003).

[5] M. Tanaka, J.P. Harbison, M.C. Park, Y.S. Park, T. Shin, and G.M. Rothberg, *J. Appl. Phys.* **76**, 6278 (1994).

[6] K. Akeura, M. Tanaka, M. Ueki, and T. Nishinaga, *Appl. Phys. Lett.* **67**, 3349 (1995).

[7] B.L. Low, C.K. Ong, J. Lin, A.C.H. Huan, H. Gong, and T.Y.F. Liew, *J. Appl. Phys.* **85**, 7340 (1999).

[8] T. Sands, J.P. Harbison, M.L. Leadbeater, S.J. Allen, Jr., G.W. Hull, R. Ramesh, and V.G. Keramidas, *Appl. Phys. Lett.* **57**, 2609 (1990).

[9] S. Sugahara and M. Tanaka, *Appl. Phys. Lett*. **80**, 1969 (2002).

[10] K.M. Krishnan, *Appl. Phys. Lett.* **61**, 2365 (1992).

[11] H. Akinaga, M. Mizuguchi, K. Ono, and M. Oshima, *Appl. Phys. Lett.* **76**, 2600 (2000).

[12] A. Continenza, S. Picozzi, W.T. Geng, and A.J. Freeman, *Phys. Rev. B* **64**,

085204 (2001).

[13] S.J. Jenkins, *Phys. Rev. B* **70**, 245401 (2004).

[14] M. Takahashi, H. Shoji, Y. Hozumi, and T. Wakiyama, *J. Magn. Magn. Mater.* **131**, 67 (1994).

[15] B.L. Low, C.K. Ong, G. C. Han, H. Gong, T.Y.F. Liew H. Tatsuoka, H. Kuwabara, and Z. Yang, *J. Appl. Phys.* **84**, 973 (1998).

[16] M. Mizuguchi, H. Akinaga, K. Ono, and M. Oshima, *Appl. Phys. Lett.* **76**, 1743 (2000).

[17] H. Tatsuoka, K. Isaji, K. Sugiura, H. Kuwabara, P.D. Brown, Y. Xin, and C.J. Humphreys, *J. Appl. Phys.* **83**, 5504 (1998).

[18] A.M. Nazmul, A.G. Banshchikov, H. Shimizu, and M. Tanaka, *J. Cryst. Growth* **227**, 874 (2001).

[19] Y. Ashizawa, S. Saito, and M. Takahashi, *J. Appl. Phys.* **91**, 8096 (2002).

[20] T. Nagao, S. Ohuchi, Y. Matsuoka, and S. Hasegawa, *Surf. Sci.* **419**, 134 (1999).

[21] H. Lippitz, J.J. Paggel, P. Fumagalli, *Surf. Sci.* **575**, 307 (2005).

[22] K.N. Tu, G. Ottaviani, R.D. Thompson, and J.W. Mayer, *J. Appl. Phys.* **53**, 4406 (1982).

[23] L. Zhang and D.G. Ivey, *J. Mater. Res.* **6**, 1518 (1991).

Chapter 5

Synthesis and magnetic properties of MnSb Nanoparticles on SiNx/Si(111) Substrates

5.1 Introduction

There have been many research activities focusing on the fabrication and characterization of magnetic nanoparticles, due to their wide range of technological applications in ultrahigh density information recording, nonvolatile memory and magnetic switch [1-4]. Considerable progress has been made in the fabrication of MnAs nanoparticles embedded in GaAs (GaAs:MnAs granular films) by annealing MBE-grown (Ga,Mn)As alloys [5-8]. The granular GaAs:MnAs films exhibit giant magnetoresistance (MR) and giant magneto-optical effects [6, 9, 10]. More than 1000% positive MR was reported in nanoscale MnSb dots grown on GaAs [5]. Akinaga *et al*. [3, 11] found that MnSb dots self-assembled on sulfur-passivated GaAs also exhibited a huge MR effect, and hence were a promising candidate for MR switch. It is highly desirable to fabricate magnetic nanoparticles with controllable and uniform sizes in device applications, since the sizes of the nanoparticles play important roles in determining their magnetization, magnetoresistivity and magneto-optical performances [10, 12]. For instance, it has been shown that the MR of granular

GaAs:MnAs material depends critically on the size of the MnAs clusters [10]. On the other hand, it is also highly desirable to fabricate the magnetic nanostructures on Si-based substrates, so that magnetic/spintronic functions can be integrated with widely-used Si-based semiconductor circuits. As shown in last chapter, Mn pnictide growth directly on Si substrates often results in interfacial Mn silicides [13, 14], which degrade the functionalities of both the substrate and the magnetic overlayer.

In this chapter, we will present the growth of MnSb nanoparticles with controllable average diameters $\langle d \rangle$ from 5 to 30 nm synthesized on ultra-thin silicon nitride covered Si(111) substrate. The ultra-thin silicon nitride layer provides a barrier against the Mn-silicide formation. MnSb particles possess sharp interfaces with Si(111) substrate. The particles with $\langle d \rangle$ = 5 and 8.5 nm are in superparamagnetic regime at room temperature, while those of $\langle d \rangle$ = 15 and 30 nm exhibit ferromagnetic behavior and desirable magnetic parameters. Since the spin injection is effective through a tunneling junction [15], ferromagnetic materials grown on a thin SiN_x dielectric layer can be utilized to make the spin-polarized electron injector in spintronic devices.

5.2 Experimental details

The growth of SiNx thin film and MnSb nanoparticles were carried out in an

ultrahigh vacuum (base pressure ~ 5×10^{-11} mbar) system equipped with STM, Auger electron spectroscopy (AES) and low-energy electron diffraction (LEED) and Ta-boat evaporators for Mn and Sb sources. Si(111)-7×7 surface was prepared by degassing the sample at 600°C for several hours followed by flashing at 1200°C for 1 minute. This procedure routinely yields a clean Si(111) as confirmed by LEED and STM. SiNx thin films were grown by nitridation of Si(111)-7×7 using high-purity NH_3 or NO at 900°C . MnSb nanoparticles were grown on the SiNx/Si(111) substrate at 250°C by simultaneously depositing Sb and Mn. The flux ratio of Sb/Mn was kept at 2-3 and the growth rate was typically 0.3 nm/min. After the growth, STM was used to study the morphology of grown MnSb nanoparticles. The chemical states and interface structures were examined with XPS and TEM. VSM and SQUID measurements were used to analyze the magnetic properties of nanoparticles with different sizes.

5.3 Results and discussion

Crystalline SiN_x thin film (~1.5 nm thick) was prepared by thermal nitridation of Si(111) using high-purity NH_3 or NO at 900°C. This nitridation process [16] results in a crystalline Si_3N_4 thin film with flat terraces and atomic steps shown in Figure 5.1(a). Si_3N_4 has been used widely as high-quality dielectric material in microelectronics. It is chemically quite inert to block the formation of

metal silicide, and makes the growth of nanoparticles thermodynamically favorable [17, 18].

By controlling deposition duration, MnSb nanoparticles of different $\langle d \rangle$ can be formed. Figure 5.1(b) shows the dependence of $\langle d \rangle$ and number density on the deposition amount. The $\langle d \rangle$ of MnSb nanoparticles (measured as the full-width at the half-maximum height in line profile) increases from 5 nm to 30 nm nearly in proportion to the deposition amount, while the nanoparticle number density decreases due to coalescence.

Figure 5.1(c) shows a STM image of MnSb nanoparticles with $\langle d \rangle$ = 8.5 nm, obtained after a deposition corresponding to a 2-nm MnSb layer. Figure 5.1(d) is the height profile along the line in Figure 5.1(c). The heights of the MnSb particles are mostly in 4.0 ± 0.5 nm range. MnSb grows in the Volmer-Weber mode, implying that MnSb has significant higher surface energies than that of SiN_x. A high density of point defects has been frequently observed on SiN_x film surfaces as reported in previous STM studies [16]. These point defects act as the nucleation sites of MnSb, so initially the density of MnSb nanoparticles can be quite high [17, 18]. With increasing deposition, MnSb nanoparticles coarsen to form larger particles, and accordingly the particle density decreases. Figure 5.1(e) shows the STM image of MnSb nanoparticles of $\langle d \rangle$ = 15 nm, obtained after a deposition corresponding to a 4-nm MnSb layer. The diameter distribution on the

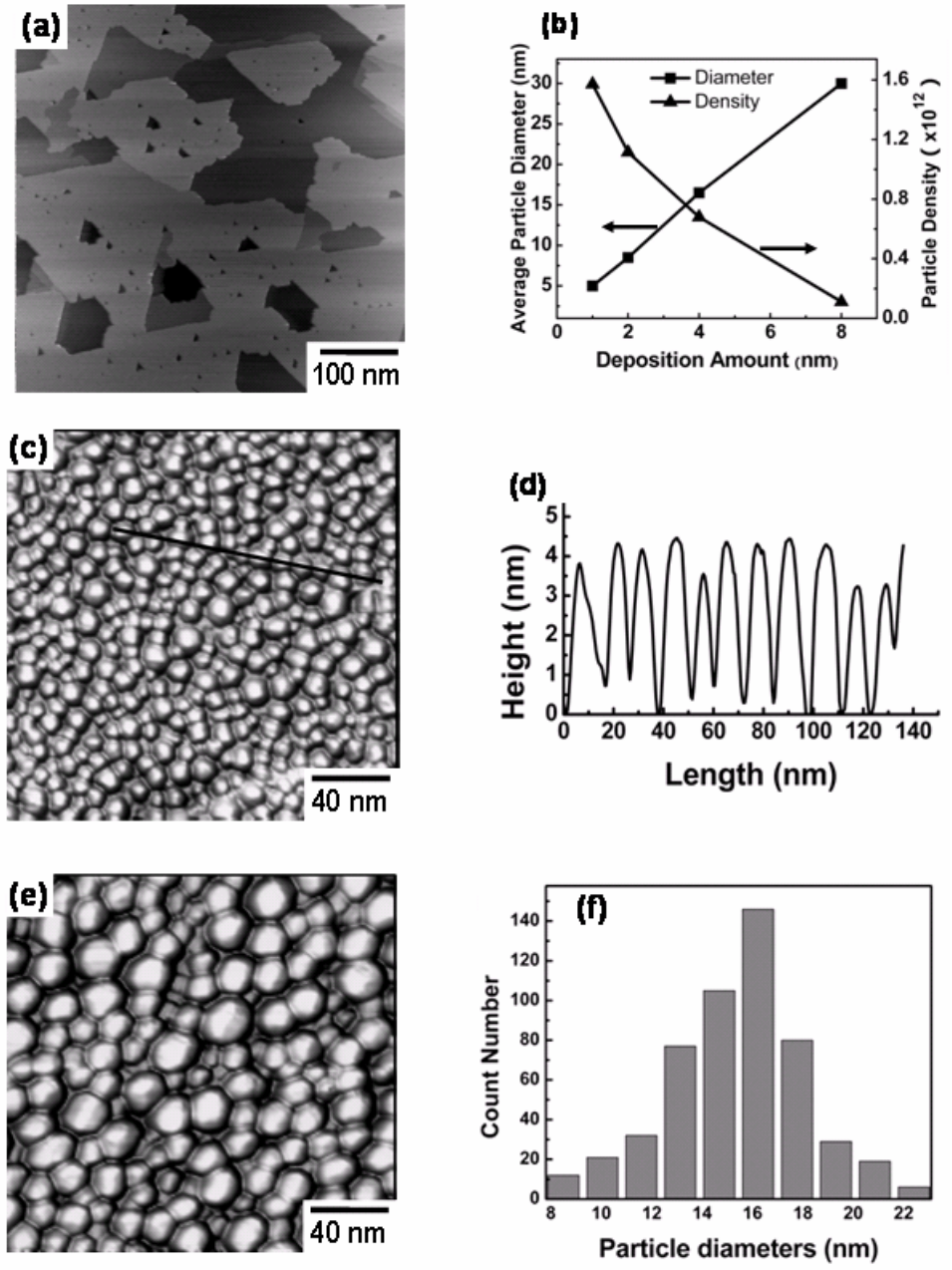

Figure 5.1 (a) STM image of crystalline Si_3N_4 thin film on Si(111); (b) plots of MnSb nanoparticle density and average diameter vs MnSb deposition amount; (c) STM image of MnSb nanoparticles with 2-nm deposition and (d) height profile along the line in (c); (e) STM image with 4-nm MnSb deposition, and (f) nanoparticle diameter distribution measured on sample in (e).

sample shown in Figure 5.1(e) has been measured statistically and is plotted in Fig. 1(f). 78% of the nanoparticles have diameters in the range of 15.5±3.0 nm.

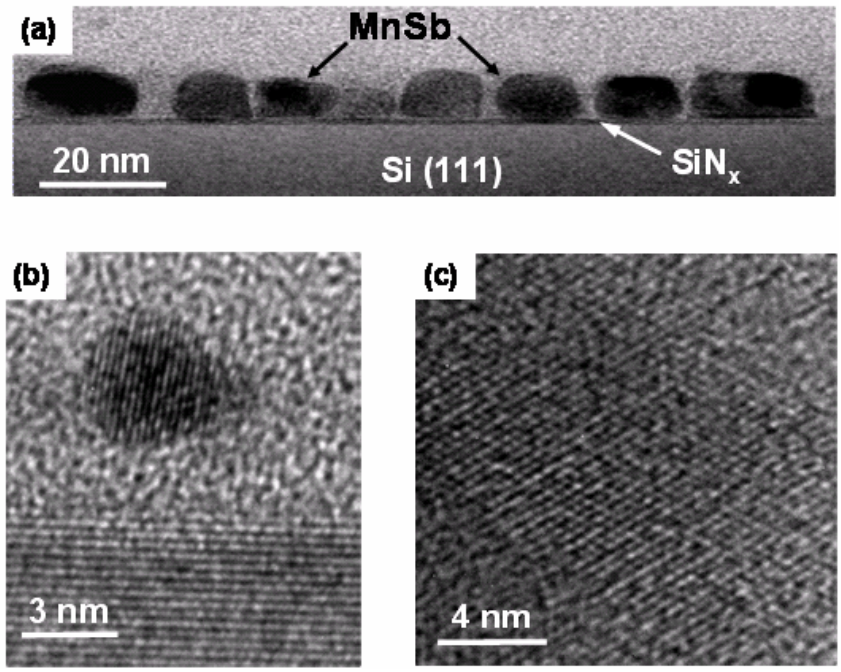

Figure 5.2 Cross-sectional TEM images of MnSb nanoparticles. (a) Large area of the sample with $\langle d \rangle$ = 15 nm; high-resolution images of MnSb crystallites with diameter of (b) 4 nm and (c) 15 nm.

It should be noted that, due to tip-shape convolution effect, the morphology of nanoparticles cannot be measured accurately, especially when they are close to one another. Thus, we also used transmission electron microscopy (TEM) to analyze the morphology, interfacial and lattice structures of the

nanoparticles. Figure 5.2(a) displays a cross-sectional TEM image of MnSb with $\langle d \rangle$ = 15 nm, which reveals an abrupt interface between MnSb and SiN_x/Si(111). MnSb, SiN_x and Si(111) regions can be distinguished clearly. This indicates that the thin Si_3N_4 film acts as an effective barrier layer against the formation of interfacial Mn silicide layer which usually occurs in Mn compound growth on Si [13, 14]. High-resolution TEM images in Figure 5.2 (b) and (c) reveal the lattice structure of the nanoparticles. The crystallite in Figure 5.2(b), with a diameter of ~ 4 nm, shows atomic planes spaced at 2.27 ± 0.08 Å, which is close to the 2.25 Å layer spacing of MnSb$(10\bar{1}2)$ [11]. The nanoparticle image in Figure 5.2(c) shows a hexagonal lattice of a period 4.12 ± 0.10 Å, which is in perfect agreement with the period on MnSb(0001). These results indicate that the nanoparticles formed on Si_3N_4 film are indeed MnSb with a NiAs-type lattice.

The chemical states and electronic structure of samples with different $\langle d \rangle$ were probed using *ex situ* X-ray photoelectron spectroscopy (XPS) and X-ray absorption spectroscopy (XAS, taken by detecting the sample current as a measure of total photoelectron yield varying with the energy of photons from a synchrotron light source). Figure 5.3(a) displays the Mn2*p* XPS spectra for samples with various $\langle d \rangle$ values. The binding energies of Mn2$p_{3/2}$ and Mn2$p_{1/2}$ are located at 641.6 eV and 653.4 eV, respectively, also confirming the formation of MnSb compound. The shake-up satellite structure around 647 eV indicates little

Mn oxide in the samples. The Mn 2*p* XAS spectra in Figure 5.3(b) show broad line shapes without clear multiplet structures. The XAS spectra are the same as that of bulk MnSb compound reported by Kimura *et al*. [19]. The broad features in XAS spectra are attributed to the itinerant Mn 3*d* electron states of NiAs-type ferromagnetic MnSb compound.

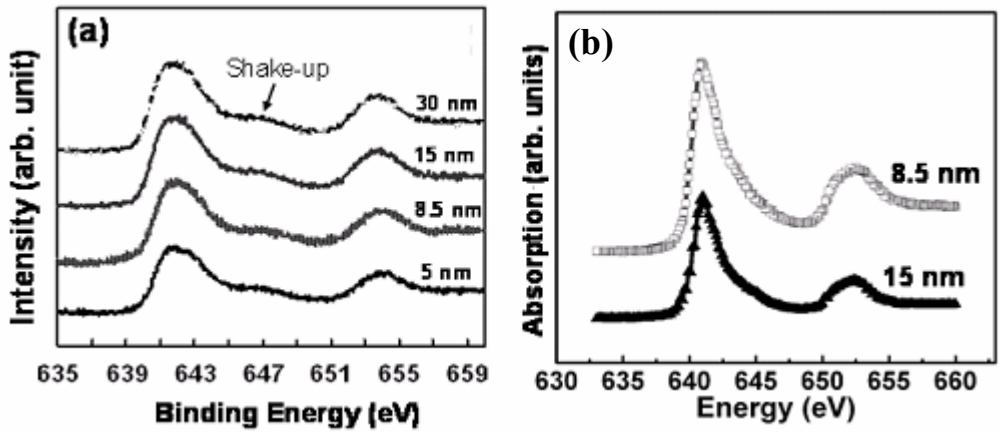

Figure 5.3 (a) Core-level XPS spectra of Mn *2p* of MnSb nanoparticles with different ⟨*d*⟩. (b) Mn 2p-3d XAS spectra of MnSb nanoparticle samples with ⟨*d*⟩ = 8.5 nm and 15 nm.

The magnetic properties of the MnSb nanoparticles were examined using vibrating sample magnetometer (VSM) and superconducting quantum interference device (SQUID) with the magnetic field applied in the plane of sample surface. The magnetization (M-H) curve of the sample with ⟨*d*⟩ = 5 nm

[Figure 5.4(a)] does not show hysteresis loop and remanent magnetization at RT, whereas at sample temperature T = 5 K a hysteresis loop was observed. The sample with MnSb particles of $\langle d \rangle$ = 8.5 nm exhibited qualitatively the same M-H curves. This suggests that the MnSb particles of these sizes are superparamagnetic at RT. The superparamagnetic behavior at T = 250 K has been reported for MnAs particles with sizes of ~ 7 nm [8].

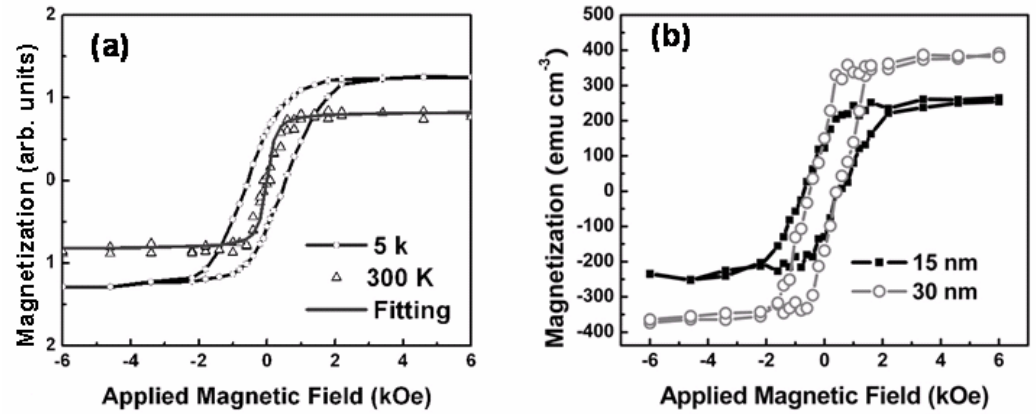

Figure 5.4 (a) Magnetization (M-H) curves of the sample of $\langle d \rangle$ = 5 nm measured by SQUID at T = 5 K (circles) and at RT (triangles), and Langevin fitting with N = 800 (gray line). (b) Magnetization curves of MnSb nanoparticles with $\langle d \rangle$ = 15 nm and 30 nm measured by VSM at RT.

The magnetization M for a superparamagnetic system can be fitted with the Langevin function:

$$M = M_S[\coth(\frac{N\mu H}{k_B T}) - \frac{k_B T}{N\mu H}]$$

where M_S is the saturation magnetization, k_B is Boltzmann constant, N is the number of Mn atoms per MnSb particle and μ is magnetic moment per Mn atom. We assume the bulk value ($\mu = 3.25\mu_B$) for Mn atoms in MnSb nanoparticles [20]. The fitting curve of the Langevin function by setting $N = 800$ agrees well with the experimental data of MnSb particles with $\langle d \rangle$ = 5 nm as shown in Figure 5.4(a). The diameter of a spherical MnSb particle of $N = 800$ is about 4 nm. As shown in TEM images, the MnSb particles are normally oblate instead of perfectly spherical, thus the particles of $N = 800$ should have lateral diameter close to 5 nm.

On the other hand, the M-H curves for the samples of $\langle d \rangle$ = 15 nm and 30 nm [Figure 5.4(b)] exhibit remanence and clear hysteresis loops at RT, indicating a ferromagnetic state of these MnSb particles. The M-H curves show that the sample of $\langle d \rangle$ = 30 nm has a smaller coercivity (H_c = 0.45 kOe) but a larger saturation magnetization ($M_S \approx 400$ emu/cm^3) than the corresponding values of the 15-nm sample (H_c = 0.65 kOe, $M_S \approx 250$ emu/cm^3). Our samples have similar M_S values but higher H_c found in the MnSb thin films which consist of μm-size crystallites [21]. The observed H_c values for our MnSb nanoparticles with $\langle d \rangle$ ~

15-30 nm make them suitable for spintronic and magnetic storage applications, due to the easy manipulation of magnetization while still maintaining a sufficient nonvolatility [8].

5.4 Conclusions

In summary, we have succeeded in the self-assembly of MnSb nanoparticles with controllable sizes on Si(111) covered with an ultra-thin SiN_x layer. TEM images display sharp interfaces and a NiAs-type lattice of the nanoparticles. The Mn 2*p* XAS spectra show broad line shapes due to the itinerant Mn 3*d* states in MnSb nanoparticles. Magnetic measurements indicate that MnSb particles with $\langle d \rangle < 9$ nm are superparamagnetic, while those with $\langle d \rangle \geq 15$ nm exhibit ferromagnetism at RT. These magnetic nanostructures offer the potential of integrating novel magnetic or spintronic functions on the widely used Si-based circuits.

References:

[1] G.A. Prinz, *Science* **250**, 1092 (1990).

[2] S. Sun, C.B. Murray, D. Weller, L. Folks, and A. Moser, *Science* **287**, 1989 (2000).

[3] H. Akinaga, M. Mizuguchi, K. Ono, and M. Oshima, *Appl. Phys. Lett.* **76**, 357 (2000).

[4] Z. Gai, G.A. Farnan, J.P. Pierce, and J. Shen, *Appl. Phys. Lett.* **81**, 742 (2002).

[5] J. De Boeck, R. Oesterholt, A. Van Esch, H. Bender, C. Bruynseraede, C. Van Hoof, and G. Borghs, *Appl. Phys. Lett.* **68**, 2744 (1996).

[6] H. Akinaga, S. Miyanishi, K. Tanaka, W. Van Roy, and K. Onodera, *Appl. Phys. Lett.* **76**, 97 (2000).

[7] M. Yokoyama, H. Yamaguchi, T. Ogawa and M. Tanaka, *J. Appl. Phys.* ***97,*** 10D317 (2005).

[8] K.Y. Wang, M. Sawicki, K.W. Edmonds, R.P. Campion, A.W. Rushforth, A.A. Freeman, C.T. Foxon, B.L. Gallagher, and T. Dietl, *Appl. Phys. Lett.* **88**, 022510 (2006).

[9] P.J. Wellmann, J.M. Garcia, J.-L. Feng, and P.M. Petroff, *Appl. Phys. Lett.* **73**, 3291 (1998).

[10] Sh.U. Yuldashev, Y. Shon, Y.H. Kwon, D.J. Fu, D.Y. Kim, H.J. Kim, T.W. Kang, and X. Fan, *J. Appl. Phys.* **90**, 3004 (2001).

[11] H. Akinaga, M. Mizuguchi, K. Ono, and M. Oshima, Appl. Phys. Lett. **76**, 2600 (2000).

[12] H. Shimizu, M. Miyamura, M. Tanaka, *Appl. Phys. Lett.* **78**, 1523 (2001).

[13] H. Tatsuoka, K. Isaji, K. Sugiura, H. Kuwabara, P.D. Brown, Y. Xin, and C.J. Humphreys, *J. Appl. Phys.* **83**, 5504 (1998).

[14] Y. Ashizawa, S. Saito, and M. Takahashi, *J. Appl. Phys.* **91**, 8096 (2002).

[15] E.I. Rashba, *Phys. Rev. B* **62**, R16267 (2000).

[16] X.-S. Wang, G. Zhai, J. Yang, L. Wang, Y. Hu, Z. Li, J.C. Tang, X. Wang, K.K. Fung, and N. Cue, *Surf. Sci.* **494**, 83 (2001).

[17] L. Wang, Y. Hu, Z. Li, J.-C. Tang, and X.-S. Wang, Nanotechnology **13**, 714 (2002).

[18] S. Gwo, C.-P. Chou, C.-L. Wu, Y.-J. Ye, S.-J. Tsai, W.-C. Lin, and M.-T. Lin, *Phys. Rev. Lett.* **90**, 185506 (2003).

[19] A. Kimura, S. Suga, T. Shishidou, S. Imada, T. Muro, S.Y. Park, T. Miyahara, T. Kaneko, T. Kanomata*, Phys. Rev. B* **56**, 6021 (1997).

[20] R. Coehoorn, C. Haas, and R.A. de Groot, *Phys. Rev.* B **31**, 1980 (1985).

[21] B.L. Low, C.K. Ong, J. Lin, A.C.H. Huan, H. Gong, and T.Y.F. Liew, *J. Appl. Phys.* **85**, 7340 (1999).